

# Gigantic second-harmonic generation and bulk photovoltaic effect in two-dimensional selenium and tellurium

Meijuan Cheng,<sup>1</sup> Zi-Zhong Zhu,<sup>1,2,\*</sup> and Guang-Yu Guo<sup>3,4,†</sup>

<sup>1</sup>*Department of Physics, Collaborative Innovation Center for Optoelectronic Semiconductors and Efficient Devices, Key Laboratory of Low Dimensional Condensed Matter Physics (Department of Education of Fujian Province), Jiujiang Research Institute, Xiamen University, Xiamen 361005, China*

<sup>2</sup>*Fujian Provincial Key Laboratory of Theoretical and Computational Chemistry, Xiamen 361005, China*

<sup>3</sup>*Department of Physics and Center for Theoretical Physics, National Taiwan University, Taipei 10617, Taiwan*

<sup>4</sup>*Physics Division, National Center for Theoretical Sciences, Hsinchu 30013, Taiwan*

(Dated: December 3, 2020)

Monolayer and few-layer tellurium films were recently prepared by molecular beam epitaxy on a graphene/6H-SiC(0001) substrate. The great breakthroughs in experiments provide a platform to explore novel two-dimensional (2D) elemental material. In this paper, a systematic first-principles study on the electronic, linear and nonlinear optical (NLO) properties of the layered selenium and tellurium within density-functional theory in the generalized gradient approximation plus scissors correction has been performed. Excitingly, layered Se and Te possess considerable second-harmonic generation (SHG), linear electro-optic (LEO) effect and bulk photovoltaic effect. In particular, trilayer Te exhibits gigantic second-order NLO susceptibility being more than 65 times larger than that of GaN, a widely used NLO material, thus indicating their potential applications in nonlinear optics. Furthermore, BL Te has huge static SHG coefficient  $\chi_{xyy}^{(2)}(0)$ , being more than 100 times larger than that of GaN. On the other hand, ML Se possesses large NLO responds with  $\chi_{xyy}^{(2)}$ , which exceeds the maximal SHG coefficient of bulk Se by 2 times and is up to six times larger than that of GaN. Remarkably, ML Se and BL Te severally possess large linear electro-optic coefficients  $r_{xyy}(0)$  and  $r_{yzx}(0)$ , which is about 6 times and 5 times larger than that of bulk GaN polytypes, respectively. In addition, we demonstrate that the TL Te exhibits huge shift current, over  $220 \mu\text{A}/\text{V}^2$ , which is 2 times greater than that of GeS, the polar system with the largest BPVE found so far. Strikingly, our work demonstrates that layered Te possess the largest Glass coefficient obtained so far in 2D noncentrosymmetric materials and the maximal Glass coefficient  $G_{xxx}$  in TL Te exceeds  $10 \times 10^{-7} \text{cm}/\text{V}$ . Interestingly, the space group of layered Se and Te strongly depends on the layer number, that is, odd and even layers corresponding to  $P2 (C_2^1)$  and  $P2_1 (C_2^2)$ , respectively. Noted that the moderate distinction between different layers systems in linear and nonlinear optical response is attributed to weak interlayer interaction. Finally, the enhanced NLO responses of 2D layered Se and Te are primarily derived from their quasi-one-dimensional structures with high anisotropy, directional covalent bonding, lone-pair electrons and band gap. These findings provide practical strategies to search for excellent NLO materials.

## I. INTRODUCTION

Noncentrosymmetric materials under intense optical fields generate large nonlinear optical responses such as second-order NLO susceptibility ( $\chi^{(2)}$ ) and third-order NLO susceptibility ( $\chi^{(3)}$ ) [1, 2]. Large second-order NLO susceptibility is of great importance for materials to apply in electro-optical switches, light signal modulators, frequency conversion, and so forth. As one of the best-known second-order nonlinear optical responses [2], the second-harmonic generation (SHG) possesses potential applications in surface probes and frequency doublers [1]. Since the 1960s, it has been investigated extensively in bulk semiconductors [2–8] and more recently also in one-dimensional [see, e.g., Refs. [9, 10] and references therein] and two-dimensional [see, e.g., Refs. [11–14] and refer-

ences therein] materials. Linear electro-optic (LEO) effect, another second-order electric polarization response of a NLO material, refers to the linear refractive index variation ( $\Delta n$ ) with the applied electric field strength ( $E$ ),  $\Delta n = n^3 r E / 2$ , where  $n$  is the refraction index and  $r$  is the LEO coefficient [2]. The LEO effect thus allows one to use an electrical signal to control the amplitude, phase, or direction of a light beam in the NLO material, and leads to a widely used means for high-speed optical modulation and sensing devices [see, e.g., Refs. [15] and references therein].

Notably, in recent years it has seen a surge of interest in the bulk photovoltaic effect (BPVE), another nonlinear optical response, referring to the generation of photovoltage or photocurrent in materials lacking inversion symmetry. Earlier studies had demonstrated intrinsic photocurrents in ferroelectric oxides  $\text{BaTiO}_3$  in 1960s [16]. Afterwards, the same photovoltaic effect had been reported for  $\text{LiNbO}_3$  [17]. In recent years, Young *et al.* demonstrated that shift current dominates the bulk photovoltaic effect in  $\text{BaTiO}_3$  from first principles calcula-

\* zzhu@xmu.edu.cn

† gyguo@phys.ntu.edu.tw

tions [18]. Then, Bhatnagar *et al.* experimentally discovered large open-circuit photovoltages and proved the bulk photovoltaic (BPV) effect in BiFeO<sub>3</sub> (BFO) [19] thin films. After this, Brehm *et al.* calculated the shift current response for polar compounds LiAsS<sub>2</sub>, LiAsSe<sub>2</sub> and NaAsSe<sub>2</sub>, and found that they exhibit shift current being up to 20 times larger than that of BiFeO<sub>3</sub> [20]. Tan *et al.* reported the bulk photocurrent response of the polar topological insulators BiTeI and CsPbI<sub>3</sub> [21]. Recently, Rangel *et al.* theoretically investigated the bulk photovoltaic effect in single-layer monochalcogenides [22]. More recently, Gong *et al.* found that ferroelectric semiconductor GeTe possesses large shift current response due to narrow band gap and high covalency [23]. As a consequence, we should turn our attention to research the bulk photovoltaic effect (BPVE) for noncentrosymmetric materials with as much as possible low band gap and high covalent bond.

As elemental materials, i.e. material systems consist of the identical element, selenium and tellurium bulks [24–28] and chains [29–37] have been investigated extensively due to their unique properties. Nevertheless, their 2D counterparts, even whole group-VI elemental 2D materials, have not been fabricated and investigated at long durations. Exhilaratingly, Qin *et al.* achieved the controlled growth of a large-size 2D selenium nanosheet using a physical vapor deposition method [38]. Zhu *et al.* revealed that the metalloid element Te exists three phases of 2D monolayer, 1T-MoS<sub>2</sub>-like ( $\alpha$ -Te) structure, tetragonal ( $\beta$ -Te) and 2H-MoS<sub>2</sub>-like ( $\gamma$ -Te) structures, named tellurene [39]. In particular,  $\beta$ -Te has been synthesized successfully on highly oriented pyrolytic graphite (HOPG) substrates by using molecular beam epitaxy [39]. Since then, extensive researches of Te-based and Se-based 2D materials have been triggered both theoretically [40–46] and experimentally [47–52]. Remarkably, in 2017, Huang *et al.* grew monolayer and few-layer Te films by molecular beam epitaxy on a graphene/6H-SiC(0001) substrate. The Te film consists of the helical chains arranged parallel exposing the Te bulk  $b-c$  (or  $a-c$ ) facet [53]. It is noteworthy that these monolayer and few-layer films without centrosymmetry are different from three structures predicted theoretically and experimentally by Zhu *et al.* [39]. Soon afterwards, several theoretical research teams investigated the structural, electronic, optical properties [54], ferroelectricity and spin-textures [55], as well as phase transitions [56] among few-layer tellurium, and so on. Strong optical absorption, high carrier mobility, outstanding environmental stability, intrinsic anisotropy, layer-dependent and almost direct bandgap were observed, indicating its potential applications in electronics, optoelectronics, vapor sensors, spintronics, biomedicine. Driven by the recently experimental breakthrough and excellent performance, in this paper, we detailedly investigate the second-harmonic generation and bulk photovoltaic effect (BPVE) of these monolayer and few-layer 2D selenium and tellurium.

The paper is organized as follows. In Sec. II, we

present the theoretical approach and computational details. In Sec. III, we report the electronic band structures of  $\alpha$ -phase layered Se and Te. In Sec. IV, we display the real and imaginary parts of the optical dielectric function. In Sec. V, the calculated LEO and SHG coefficients over the entire optical frequency range are investigated. Furthermore, the second-order optical susceptibility are analyzed in terms of one- and two-photon resonances via the calculated absorptive parts of the dielectric function. In Sec. VI, we systematically investigate the shift current (SHC) response, photoresponsivity as well as Glass coefficient. Comparison of the obtained results of the materials with the known NLO materials suggests that 2D selenium and tellurium possess potential applications in nonlinear optical devices such as novel solar-cell, photodetector, SH generation, electro-optical modulator and electric optical switches, and so on. In Sec. VII, we research deformation charge density to investigate the origins of the enhanced NLO responses of selenium and tellurium. Finally, a summary is given in Sec. VIII.

## II. STRUCTURE AND COMPUTATIONAL METHOD

The ball-stick structure of bulk selenium and tellurium ( $\alpha$ -phase) is schematically shown in Figs. 1(a), 1(b) and 1(c). It consists of parallel-aligned helical chains arranged in a hexagonal array [57, 58]. Every atom is covalently bonded to two neighboring atoms along each chain, and interacts weakly with atoms of the adjacent chains. Clearly, bulk selenium and tellurium ( $\alpha$ -phase) may be viewed as layered structure showed in Fig. 1(a). The different layers are stacked in the direction perpendicular to  $a-c$  (or  $b-c$ ) planes, while each layer is single helical chain stretched to infinity along the  $c$  axis direction. The few-layer structures consist of  $n$  helical chains stacked in a bulk mode [see Figs. 1(d), 1(e) and 1(f)]. Here,  $n$  denotes the number of layers. Interestingly, space group of odd layers structures is  $P2$  ( $C_2^1$ ), while that of even layers structures corresponds to  $P2_1$  ( $C_2^2$ ) (see Table II). It's worth noting that  $\alpha$ -phase monolayer and few-layer structures all possess broken inversion symmetry, the necessary condition for second-order nonlinear optical effects. However, for tellurium, when the thickness of these layered structures named  $\alpha$ -phase reduces to the monolayer limit, the  $\alpha$ -phase is unstable against a transition into  $\beta$ -phase [see Figs. 1(g), 1(h) and 1(i)], a structure with centrosymmetry. That is,  $\beta$ -phase is the most stable monolayer phase for ML tellurium, while for all layered (ML and few-layer) Se and few-layer Te,  $\alpha$ -phase is more stable than other phases. As reported in previous work [55], lone-pair interactions between the layers for bilayer  $\beta$  structure induce phase transition into non-centrosymmetric  $\alpha$ -phase, a structure the same as the  $\alpha$  phase bulk. Consequently, we perform a systematic ab initio density functional investigation of the linear and nonlinear optical properties for  $\alpha$ -phase 2D selenium

and tellurium, namely layered (ML, BL and TL) Se and multilayer (BL and TL) Te. Table II shows that the distances of intrachain  $r$  for layered Se are smaller than that of bulk counterpart, implying stronger covalent interaction between the nearest atoms and then larger NLO responses, as will be explained in Sec. VII below. Although some bond lengths of  $\alpha$ -phase multilayer Te are larger than bulk Te (see Table II), but in general, the increase is diminutive compared to the decrement, indicating a generally enhanced intrachain interaction in these low-dimensional systems. In the present calculations, the layered structures are modeled by using the slab-superlattice approach with the separations between MLs being about 20 Å, ensuring negligible interaction between the periodic images.

TABLE I. Calculated with SCAN, optB88-vdW, DFT-D2, PBE functionals and experimental lattice constants for selenium and tellurium bulks.

		SCAN	optB88-vdW	PBE-D2	PBE	exp
Se	<i>a</i>	4.4336	4.2348	4.2517	4.4984	4.3662 <sup>a</sup>
	<i>c</i>	4.9984	5.1319	5.1065	5.0526	4.9536 <sup>a</sup>
Te	<i>a</i>	4.4578	4.4816	4.3357	4.5085	4.4511 <sup>b</sup>
	<i>c</i>	5.9291	5.9951	6.0300	5.9593	5.9262 <sup>b</sup>

<sup>a</sup>Experimental value from reference 57.

<sup>b</sup>Experimental value from reference 58.

Ab initio calculations are performed using the highly accurate projector augmented wave (PAW) method [59], as implemented in the VASP package [60, 61]. They are based on density functional theory with the generalized gradient approximation (GGA) of Perdew, Burke, and Ernzerhof [62]. A large plane-wave cutoff energy of 450 eV is used throughout. Test calculations using  $E_{cut} = 500$  eV for selenium monolayer yields the band structure being identical to that of  $E_{cut} = 450$  eV. The PAW potentials are adopted to describe the electron-ion interaction, with six valence electrons for Se ( $4s^2 4p^4$ ) and also for Te ( $5s^2 5p^4$ ). The theoretical atomic positions and lattice constants were obtained when the forces acting on all the atoms are less than 0.001 eV/Å and the stresses are less 1.0 kBar, respectively. The total energy convergence criterion for the self-consistent electronic structure calculations is  $10^{-6}$  eV. The accurate tetrahedron method [63] is used for the Brillouin zone integration. The self-consistent charge density calculations are performed with k-point meshes of  $18 \times 20 \times 1$  for layered Se,  $15 \times 20 \times 1$  for multilayer Te, respectively. Further calculations using different k-point meshes indicate that the above k-point meshes produce the well-converged charge density.

To obtain accurate structure parameters, firstly, we perform structural optimizations of the atomic positions and lattice constants for bulk selenium and tellurium with the conjugate gradient technique considering van der Waals interactions using SCAN [64, 65], optB88-vdW [66], Perdew-Burke-Ernzerhof (PBE) [62], DFT-D2 [67] functionals, respectively. The calculated lattice con-

stants based on SCAN functional agree rather well with that of experiments [57, 58] compared to other theoretical calculations (see Table I). Therefore, in geometric optimization calculations, we adopt the SCAN functional for layered 2D structures, which was verified to be of sufficient accuracy in describing the structural properties of layered materials [54], to improve the description of van der Waals interactions between atomic chains. In all the subsequent calculations, we use the SCAN functional theoretically determined layered atomic structures.

In this work, the optical dielectric function and SHG coefficient are calculated based on the linear response formalism with the independent-particle approximation, as described previously [8, 9, 68]. The imaginary part of the dielectric function  $\epsilon(\omega)$  due to direct interband transition is given by the Fermi golden rules [see, e.g., Refs. [9, 68]],

$$\epsilon''_a(\omega) = \frac{4\pi^2}{\Omega\omega^2} \sum_{i \in VB, j \in CB} \sum_k w_k |p_{ij}^a|^2 \delta(\epsilon_{\mathbf{k}j} - \epsilon_{\mathbf{k}i} - \omega), \quad (1)$$

where  $\Omega$  is the unit-cell volume and  $\omega$  is the photon energy. VB and CB stand for the valence and conduction bands, respectively. The dipole transition matrix elements  $p_{ij}^a = \langle \mathbf{k}j | \hat{p}_a | \mathbf{k}i \rangle$ , where  $\hat{p}_a$  represents Cartesian component  $a$  of the dipole operator, are obtained from the self-consistent band structures within the PAW formalism [69]. Here  $|\mathbf{k}n\rangle$  is the  $n$ th Bloch state wave function with crystal momentum  $\mathbf{k}$  and  $a$  represents the cartesian components. The real part of the dielectric function is then obtained from the calculated  $\epsilon''(\omega)$  by the Kramer-Kronig transformation [9, 68],

$$\epsilon'(\omega) = 1 + \frac{2}{\pi} \mathbf{P} \int_0^\infty d\omega' \frac{\omega' \epsilon''(\omega')}{\omega'^2 - \omega^2}. \quad (2)$$

Where  $\mathbf{P}$  denotes the principal value of the integral.

The imaginary part of the second-order optical susceptibility due to direct interband transitions is given by [9, 10]

$$\chi_{abc}^{(2)}(-2\omega, \omega, \omega) = \chi_{abc,VE}^{(2)}(-2\omega, \omega, \omega) + \chi_{abc,VH}^{(2)}(-2\omega, \omega, \omega), \quad (3)$$

where the contribution due to the so-called virtual-electron (VE) process is [9, 10]

$$\begin{aligned} \chi_{abc,VE}^{(2)} = & -\frac{\pi}{2\Omega} \sum_{i \in VB} \sum_{j,l \in CB} \sum_{\mathbf{k}} w_{\mathbf{k}} \left\{ \frac{\text{Im}[p_{jl}^a \langle p_{li}^b p_{ij}^c \rangle]}{\epsilon_{li}^3(\epsilon_{li} + \epsilon_{ji})} \delta(\epsilon_{li} - \omega) \right. \\ & \left. - \frac{\text{Im}[p_{ij}^a \langle p_{jl}^b p_{li}^c \rangle]}{\epsilon_{li}^3(2\epsilon_{li} - \epsilon_{ji})} \delta(\epsilon_{li} - \omega) + \frac{16\text{Im}[p_{ij}^a \langle p_{jl}^b p_{li}^c \rangle]}{\epsilon_{ji}^3(2\epsilon_{li}^3 - \epsilon_{ji}^3)} \delta(\epsilon_{ji} - 2\omega) \right\}, \end{aligned} \quad (4)$$

and that due to the virtual-hole (VH) process is [9, 10]

$$\begin{aligned} \chi_{abc,VH}^{(2)} = & \frac{\pi}{2\Omega} \sum_{i,l \in VB} \sum_{j \in CB} \sum_{\mathbf{k}} w_{\mathbf{k}} \left\{ \frac{\text{Im}[p_{li}^a \langle p_{ij}^b p_{jl}^c \rangle]}{\epsilon_{jl}^3(\epsilon_{jl} + \epsilon_{ji})} \delta(\epsilon_{jl} - \omega) \right. \\ & \left. - \frac{\text{Im}[p_{ij}^a \langle p_{jl}^b p_{li}^c \rangle]}{\epsilon_{jl}^3(2\epsilon_{jl} - \epsilon_{ji})} \delta(\epsilon_{jl} - \omega) + \frac{16\text{Im}[p_{ij}^a \langle p_{jl}^b p_{li}^c \rangle]}{\epsilon_{ji}^3(2\epsilon_{jl} - \epsilon_{ji})} \delta(\epsilon_{ji} - 2\omega) \right\}. \end{aligned} \quad (5)$$

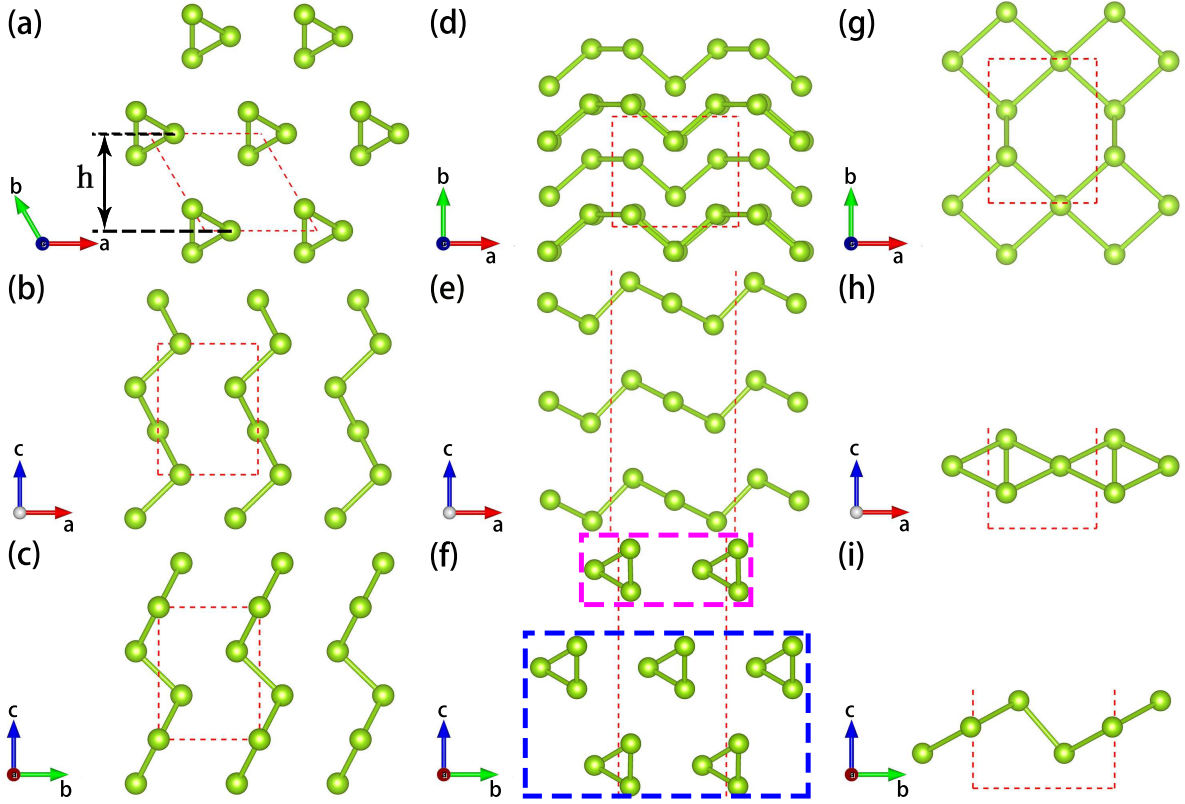


FIG. 1. Crystalline structure of bulk selenium and tellurium in the (a) top and [(b) and (c)] side views. (d) Top and [(e) and (f)] side views of trilayer (TL)  $\alpha$ -Se or  $\alpha$ -Te structures. In (a), the symbol  $h$  is the effective thickness of one monolayer structure. In (f), the blue dashed rectangle indicates corresponding bilayer (BL)  $\alpha$ -Se or  $\alpha$ -Te structures. The magenta dashed rectangle indicates corresponding monolayer (ML)  $\alpha$ -Se structure. (g) Top and [(h) and (i)] side views of monolayer (ML)  $\beta$ -Te. The red dashed lines indicate the unit cell of each structure.

TABLE II. Space group, the distance of intrachain  $r$ , effective thickness  $h$  and calculated lattice constants  $a$ ,  $b$  and  $c$  with SCAN functional for bulk and layered selenium and tellurium.

	Se bulk	Se ML	Se BL	Se TL	Te bulk	Te BL	Te TL
space group	$P3_121$	$P2$	$P2_1$	$P2$	$P3_121$	$P2_1$	$P2$
$r$	2.38	2.35/2.37	2.36/2.38	2.36/2.37/2.38	2.86	2.79/2.87/2.89	2.80/2.83/2.84/2.88
$h$		3.781	7.562	11.344		7.710	11.564
$a$	4.434	4.918	4.955	4.968	4.458	5.791	5.839
$b$	4.434	4.198	4.287	4.336	4.458	4.311	4.367
$c$	4.998				5.929		

Here  $\epsilon_{ji} = \epsilon_{kj} - \epsilon_{ki}$  and  $\langle p_{jl}^b p_{li}^c \rangle = \frac{1}{2}(p_{jl}^b p_{li}^c + p_{li}^b p_{jl}^c)$ . The real part of the second-order optical susceptibility is obtained from the calculated  $\chi_{abc}''^{(2)}$  by the Kramer-Kronig transformation [9, 10]

$$\chi^{(2)}(-2\omega, \omega, \omega) = \frac{2}{\pi} \mathbf{P} \int_0^\infty d\omega' \frac{\omega' \chi''^{(2)}(2\omega', \omega', \omega')}{\omega'^2 - \omega^2}. \quad (6)$$

The linear electro-optic coefficient  $r_{abc}(\omega)$  is related to the second-order optical susceptibility  $\chi_{abc}^{(2)}(-\omega, \omega, 0)$  [5].

In the zero frequency limit,

$$r_{abc}(0) = -\frac{2}{\epsilon_a(0)\epsilon_b(0)} \lim_{\omega \rightarrow 0} \chi_{abc}^{(2)}(-2\omega, \omega, \omega). \quad (7)$$

In the very low frequency region, i.e. the photon energy  $\hbar\omega$  well below the band gap,  $\chi_{abc}^{(2)}(-2\omega, \omega, \omega)$  and  $n(\omega)$  are nearly constant. In this case, the LEO coefficient  $r_{abc}(\omega) \approx r_{abc}(0)$  [9, 11].

Shift current is regarded to be one of the major origins of the bulk photovoltaic effect. Therefore, in our work, we

calculate the shift current by the following equation[22],

$$J_a(\omega) = 2 \sum_{bc} \sigma_{abc}(0; \omega, -\omega) E_b(\omega) E_c(-\omega). \quad (8)$$

Where the third-rank tensor  $\sigma_{abc}(0; \omega, -\omega)$  could be expressed as[22]

$$\sigma_{abc}(0; \omega, -\omega) = -\frac{i\pi e^3}{2\hbar^2} \int \frac{d\mathbf{k}}{8\pi^3} \sum_{nm} f_{nm} (r_{mn}^b r_{nm;a}^c + r_{mn}^c r_{nm;a}^b) \delta(\omega_{mn} - \omega). \quad (9)$$

Here  $r_{mn}^a$  denote velocity matrix elements. The generalized derivatives  $r_{mn;b}^a = \partial r_{mn}^a / \partial k^b - i(A_{nn}^b - A_{mm}^b) r_{nm}^a$ . Where  $A_{nm}^a$  are the Berry connections.

The photoresponsivity  $k_{abb}$  is the current density generated per incident intensity. That is  $k_{abb} = \frac{J_a}{I_{0,b}}$ [70]. Polarization intensity  $I_{0,b}$  is expressed by  $I_{0,b} = \frac{c\epsilon_0 |E_b|^2}{2}$ [70]. Accounting for the form of shift current from equation (8), the photoresponsivity  $k_{abb}$  can be expressed by

$$k_{abb} = \frac{4\sigma_{abb}}{c\epsilon_0} \quad (10)$$

Where  $\epsilon_0$  is the vacuum permittivity and  $c$  is the speed of light.

Glass coefficient, another important quantity of bulk photovoltaic effect (BPVE), denotes the photocurrent of a thick sample considering the incident-light penetration depth, which can be calculated by  $G_{abb}(\omega) = \frac{\sigma_{abb}(\omega)}{\alpha_{bb}(\omega)}$ [22]. Then we take the relationship between shift current  $J$  and Glass coefficient  $G$  into account, i.e.  $J = G_{abb} \alpha_{bb}(\omega) I$ , Glass coefficient can be expressed as

$$G_{abb}(\omega) = \frac{k_{abb}(\omega)}{\alpha_{bb}(\omega)}. \quad (11)$$

Here  $\alpha_{bb}$  is the absorption coefficient.

In the present calculations, the function  $\delta$  in Eqs. (1), (4) and (5) is approximated by a Gaussian function with  $\Gamma = 0.2$  eV. Furthermore, to obtain accurate optical properties, we perform calculations for selenium and tellurium with several different  $k$ -point meshes until the calculated optical properties converge to a few percent. Therefore, adequately dense  $k$ -point meshes of  $52 \times 60 \times 1$  and  $45 \times 60 \times 1$  are adopted for selenium and tellurium, respectively. In particular, 30 energy bands per atom are included in the present optical calculations in order to ensure that  $\epsilon'$  and  $\chi^{(2)}$  calculated by the Kramer-Kronig transformation are reliable, as confirmed by further test calculations for monolayer selenium using different numbers of bands. The unit cell volume  $\Omega$  in Eqs. (1), (4) and (5) is not well-defined for these layered 2D Se and Te in the slab-supercell approach. Therefore, we adopt the effective unit cell volume, which is given by the area of the in-plane unit cell times the effective thickness  $h$  (see Table II), rather than the volume of the supercells

that is arbitrary. Here, the effective thickness is set to  $n$  times the interlayer distance of corresponding bulks [see Fig. 1(a)].

We should note that the linear and nonlinear optical properties calculated via Eqs. (1), (4) and (5) are on the basis of the independent-particle approximation (IPA), that is, the quasi-particle self-energy corrections and excitonic effects are neglected. These many-body effects on the optical properties of 2D systems such as ML SiC and MoS<sub>2</sub> [71, 72] are pronounced due to quantum confinement. However, in this work, we take the self-energy corrections into account by the scissors correction (SC) [73] using the band gaps from the hybrid functional HSE06 [74] calculations, which is known to produce much improved band gaps for semiconductors (see Table III below). The so-called SC calculation, that is to say, the conduction bands are consistently upshifted so that the band gap would match the accurate HSE gap together with the renormalized transition matrix elements [73]. Indeed, such SC calculations were proved to be considerably accurate for low-dimensional materials such as graphene-like BN sheet which agrees well with the experimental one [11]. It is well known that weak or moderate electron-hole interaction would simply enhance the peaks near the absorption edge such as GaAs [75]. While, strong electron-hole interaction may come into being additional obvious excitonic peaks below the absorption edge such as MoS<sub>2</sub> ML [72]. Nevertheless, multilayer Se and Te possess sufficient thickness and then one could expect no strong excitonic effect on their optical properties. Furthermore, as reported in a very recent experiment, there was no excitonic transition peak observed in ultrathin GaSe films with indirect band gap. Similar to GaSe films, indirect-band-gap monolayer Se is supposed to no strong electron-hole interaction.

### III. ELECTRONIC BAND STRUCTURE

TABLE III. Calculated ( $E_g^{GGA}$  and  $E_g^{HSE-SOC}$ ) and experimental band gap ( $E_g^{Exp}$ ) as well as scissors operator ( $\Delta E_g = E_g^{HSE-SOC} - E_g^{GGA}$ ) for layered selenium and tellurium. The values in brackets are previous HSE calculations with the SOC.

	$E_g^{GGA}$ (eV)	$E_g^{HSE-SOC}$ (eV)	$E_g^{Exp}$ (eV)	$\Delta E_g$ (eV)
Se ML	1.885	2.641		0.756
BL	1.526	2.270		0.744
TL	1.335	2.078		0.743
Te BL	0.997	1.286(1.17) <sup>a</sup>	0.85 <sup>b</sup>	0.289
TL	0.773	1.072(0.95) <sup>a</sup>	0.74 <sup>b</sup>	0.299

<sup>a</sup>Theoretical value from reference 54.

<sup>b</sup>Experimental value from reference 53.

To understand the electronic and optical properties of the  $\alpha$ -phase layered Se and Te, we calculate their electronic band structures (see Fig. 2). It is clear from Fig.

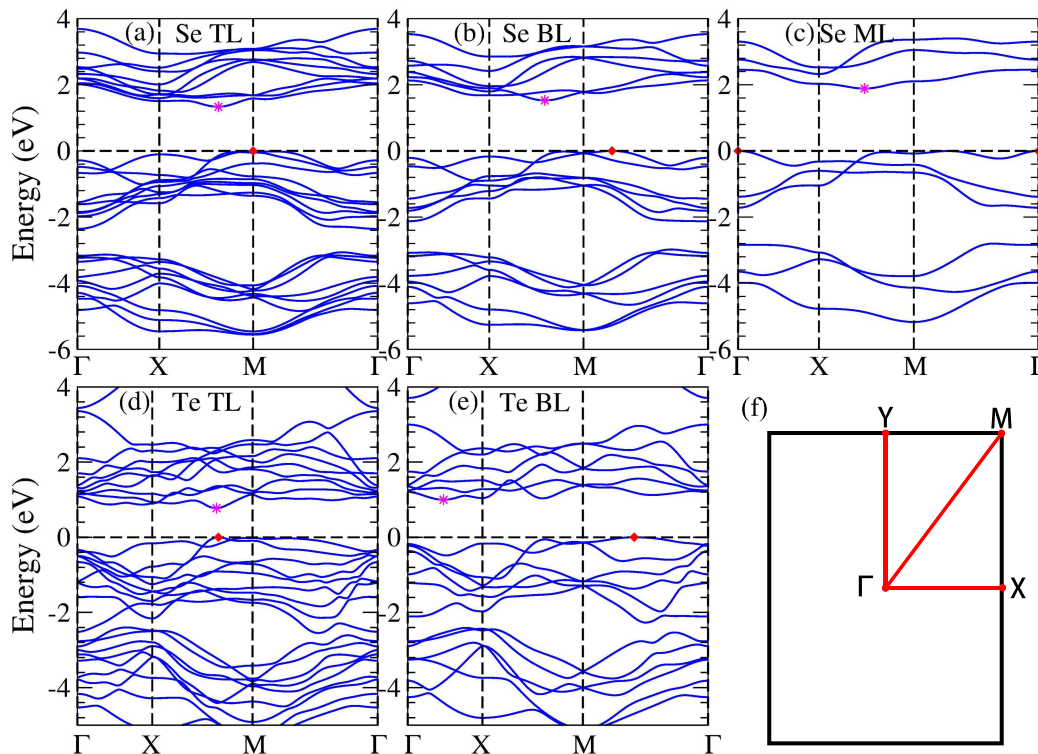


FIG. 2. Band structures of layered (a), (b) and (c) selenium as well as (d) and (e) tellurium. The valence band maximum (VBM) is marked as a red diamond, while the conduction band minimum (CBM) is indicated by magenta star. (f) Two-dimensional Brillouin zone. Both materials possess an indirect band gap. The top of the valence bands is at 0 eV.

2 that all layered Se and BL Te are indirect band-gap semiconductors, while TL Te is nearly direct band-gap. For bilayer tellurium, the valence band maximum (VBM) is relatively close to the M point along the M- $\Gamma$  direction while conduction band minimum (CBM) is located somewhere slightly closed to  $\Gamma$  along the  $\Gamma$ -X symmetry line. Excitingly, if the thickness of few-layer tellurium increases to thilayer, both of VBM and CBM are located at general k-point closed to M along the X-M direction, that is, thilayer (TL) tellurium is considered as a nearly direct band gap semiconductor and thus could be expected to possess potential applications in semiconductor devices. The transition origin of band gap for tellurium from an indirect character to nearly direct one as the thickness of layers increasing is nearly direct band-gap nature of Te bulk. A opposite transition of band-gap character has been found in 2D MoS<sub>2</sub> [76]. Furthermore, the theoretical band gaps from the GGA and HSE calculations together with the experimental values are also listed in Table III. Obviously, the band gap we calculated with HSE considering SOC is 1.286 (1.072) eV in BL (TL) tellurium, which agrees rather well with the result of Ref. [54] (see Table III). The small difference stems from the fact that the calculated band gap for Ref. [54] are based on the optB88-vdW structure, while we use the structures from SCAN functional. Furthermore, likely due to graphene substrate, the band gap measured in the ex-

periment for multilayer Te is smaller than the ones calculated via the hybrid functional considering spin orbit interaction. Interestingly, when the thickness of layered selenium increases from monolayer limit to thilayer, the location of valence band maximum (VBM) moves from symmetry point  $\Gamma$  to M along  $\Gamma$ -M symmetry line. The conduction band minimum (CBM) is always located at a general k-point along the X-M symmetry line. Nevertheless, it is getting closer and closer to M symmetry point with the increase of thickness [see Figs. 2(a), (b) and (c)]. Clearly, the band gap of 2D selenium is larger than that of corresponding layered tellurium due to the increased ionization energy (see Table III). In general, the band gap of 2D layered Se and Te are tunable depending on the number of layers. In particular, the accurate gap of BL Te from HSE-SOC calculations is close to 1.3 eV, the ideal gap value [77]. Therefore, one could expect BL Te to produce extremely high power conversion efficiency in photovoltaic devices.

It is well known that the band gap of semiconductor is generally underestimated by the generalized gradient approximation (GGA) calculations. As mentioned before, to obtain more accurate band gaps, we also calculate the band structures by using the hybrid Heyd-Scuseria-Ernzerhof (HSE) functional [74]. The band structures from the HSE calculations with the SOC included are displayed in Fig. S1. Additionally, the theoretical band

gaps from the GGA and HSE calculations together with the experimental values are listed in Table III. Indeed, the band gaps from the HSE calculations with the SOC included were proved to be highly accurate in describing band gap in our very recent report [8]. Therefore, we use the band gap differences between the HSE-SOC calculations and GGA calculations as the scissors correction energy [73] to evaluate linear and NLO properties for  $\alpha$ -phase 2D layered Se and Te.

#### IV. LINEAR OPTICAL PROPERTY

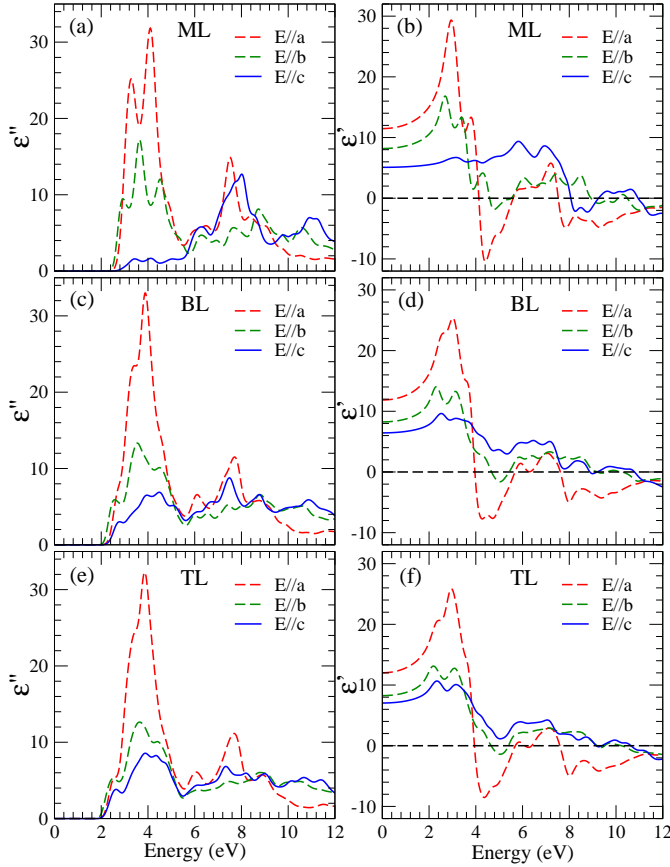


FIG. 3. The imaginary [ $\epsilon''(\omega)$ ] and real part [ $\epsilon'(\omega)$ ] of the dielectric function for (a) and (b) ML selenium, (c) and (d) BL selenium as well as (e) and (f) TL selenium for both light polarization perpendicular ( $E \parallel a$  and  $E \parallel b$ ) and parallel ( $E \parallel c$ ) to the  $c$  axis.

In Fig. 3 and Fig. 4, the calculated real and imaginary parts of the optical dielectric function  $\epsilon(\omega)$  of layered selenium and tellurium are shown. In contrast to bulk counterparts, hexagonal lattice, 2D layered Se and Te exhibit rectangular lattice [see Fig. 1(d)], resulting in stronger dependence of optical properties on light polarization direction. Therefore, the real and imaginary parts of the dielectric function for ML and few-layer Se

and multilayer Te compose of three significantly different components, i.e., light polarization parallel ( $E \parallel c$ ) and perpendicular ( $E \parallel a$  and  $E \parallel b$ ) to the  $c$  axis. Strikingly, all 2D Se and Te exhibit stronger optical anisotropy than their bulk counterparts. Compared to bilayer and thilayer selenium, the spectra of real and imaginary parts of the optical dielectric function  $\epsilon(\omega)$  of monolayer selenium possess sharper peaks (see Fig. 3). For example, Fig. 3(a) shows rather sharp peaks near 3.3 eV for  $E \parallel a$  and 8.0 eV for  $E \parallel c$  which, however, appears only as slightly weaker shoulder and bulge in the spectra of  $\epsilon''(\omega)$  of corresponding bilayer [Fig. 3(c)] and thilayer materials [Fig. 3(e)]. This difference may be caused by weak quantum confinement effects in the monolayer selenium. Furthermore, Fig. 3(a) shows that there is very weak optical absorption for  $E \parallel c$  in the low-energy region (about 2.5-5.5 eV). Nevertheless, the absorption increases with layer increment [Fig. 3(c) and Fig. 3(e)]. It could be interpreted as the result of weak interactions between layers. Overall, in the low-energy region (about 2.5-5.5 eV), the optical anisotropy is more remarkable for all layered selenium. In the high-energy region (about 5.5-12 eV), for  $E \parallel a$ , there is a prominent peak and two shoulder peaks for all the systems. For  $E \parallel b$  and  $E \parallel c$ , the amplitude of peaks gradually decreases with layer increment. Additionally, these peaks become some steadily oscillatory bulges in multilayer selenium, particularly in TL selenium. This could be explained by the fact that there are weak interaction in the interchain and between layers, respectively. In particular, the spectra of real and imaginary parts of the optical dielectric function  $\epsilon(\omega)$  for BL and TL systems are rather similar except the spectra for  $E \parallel c$  (direction of layers). This also could be explained as result of the weak interlayer interaction in layered materials. The same phenomenon has been observed in  $\text{Cr}_2\text{Ge}_2\text{Te}_6$  [78]. It is noted that the optical spectra for  $E \parallel a$  (parallel to the chains direction) and  $E \parallel c$  (direction of layers) of thilayer selenium are extremely similar to the corresponding spectra of bulk counterpart [8].

For bilayer and thilayer tellurium, the positions and amplitude of peaks possess significant difference especially for  $E \parallel c$  (direction of layers) indicating stronger interlayer interaction than layered selenium. However, similarly, with the thickness of layers increase, the spectra of real and imaginary parts of the optical dielectric function  $\epsilon(\omega)$  seem more like bulk counterpart. Fig. 4(c) shows that there is a pronounced peak at  $\sim 1.9$  eV for  $E \parallel a$  and  $E \parallel b$ . Furthermore, For  $E \parallel c$ , the spectrum of imaginary part of the optical dielectric function for TL tellurium exhibits a prominent peak near 2.8 eV. Strikingly, a deep minimum occurs at  $\sim 4.4$  eV for light polarization parallel to the  $c$  axis and this could be explained by the fact that transitions from the upper valence bands to the lower conduction bands are already exhausted. Then, the spectral amplitude increases within the energy range between 4.4 eV and 7.5 eV due to the transitions from the lower valence bands to the lower con-

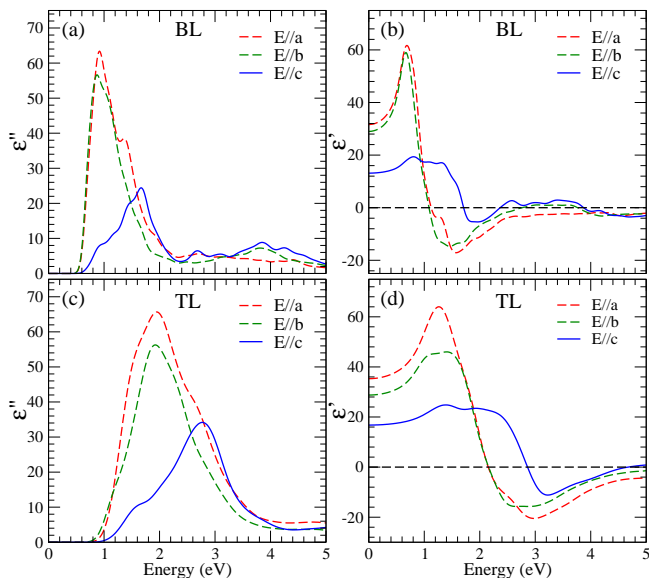


FIG. 4. The imaginary  $[\varepsilon''(\omega)]$  and real part  $[\varepsilon'(\omega)]$  of the dielectric function for (a) and (b) BL tellurium as well as (c) and (d) TL tellurium for both light polarization perpendicular ( $E||a$  and  $E||b$ ) and parallel ( $E||c$ ) to the  $c$  axis.

duction bands and also from the upper valence bands to the upper conduction bands. Overall, the optical absorption, a crucial factor to enhance the efficiency of a solar cell, exists in a relatively wide range of energy for bilayer and trilayer Te. Compared to BL Te, TL Te exhibits enhanced optical absorption properties due to nearly-direct band gap, indicating that TL Te would be advanced candidates for next generation optoelectronic devices.

## V. SECOND HARMONIC GENERATION AND LINEAR ELECTRO-OPTIC EFFECT

The calculated static dielectric constant  $\varepsilon(0)$ , second-order NLO susceptibility  $\chi^{(2)}(0,0,0)$  and zero-frequency LEO coefficient  $r(0)$  without (IPA) and with (SCI) scissors correction are presented in Table IV and V. As mentioned before [8], the line shapes of dielectric function and the SHG susceptibility from the two types of calculations, i.e. GGA and SCI, are nearly identical, while the magnitude of these linear and nonlinear optical effects from the scissors correction calculations is reduced (see Table IV and V) and the peak positions are blue-shifted by about scissors correction energy ( $\Delta E_g$ ). Therefore, in this paper, we only discuss the static values and spectra of the linear and nonlinear optical effects obtained from the scissors corrected band structures. Bulk selenium and tellurium have five nonzero nonlinear susceptibility since their symmetry class is  $D_3^4$  or  $D_3^6$  (right-handed or left-handed screw) without the spatial inversion symmetry. However, layered selenium and tellurium possess lower symmetry signifying more nonzero susceptibility

elements emerging. Interestingly, as mentioned above, the space group significantly depends on the layer, i.e. odd and even layers corresponding to  $P2$  ( $C_2^1$ ) and  $P2_1$  ( $C_2^2$ ), respectively. However, the two space groups possess identical independent elements. That is, all layered selenium and tellurium would exhibit the second-order nonlinear optical response with nonzero susceptibility elements  $\chi_{xxx}^{(2)}$ ,  $\chi_{xyy}^{(2)}$ ,  $\chi_{xyx}^{(2)}$ ,  $\chi_{zzy}^{(2)}$ ,  $\chi_{zyz}^{(2)}$ ,  $\chi_{zyx}^{(2)}$ ,  $\chi_{zzx}^{(2)}$  and  $\chi_{xzz}^{(2)}$ .

### A. Layered Se

Interestingly, the anisotropy of static  $\varepsilon(0)$  is strong in all the 2D layered materials studied here. The same phenomenon is observed in the static second-order NLO susceptibility and the LEO coefficient (see Table IV and V). Remarkably, ML Se exhibits large linear electro-optic coefficients  $r_{xyy}$  ( $\sim 3.29$  pm/V), which is nearly 6 times larger than that of bulk GaN polytypes [6, 7]. The real and imaginary parts of the second-order susceptibility for monolayer selenium are displayed in Fig. 5, while that of bilayer and trilayer selenium are shown in Fig. S2 and Fig. S3 in the SM. Overall, the calculated optical spectra of the SHG coefficients for all layered Se are rather similar (see Figs. 5, S2 and S3) due to the weak interlayer interaction. Therefore, in what follows, we will take that of ML selenium as example to perform a detailed analysis.

Fig. 5 indicates that the spectra of all second-order susceptibility are purely dispersive for photon energy being smaller than half of band gap, indicating that ML selenium has potential application in nonlinear optical devices. Furthermore, the second-order susceptibility  $\chi_{xyy}^{(2)}$  is larger in the entire range of optical photon energy than the rest of nonzero elements. Hence, in what follows, we only take  $\chi_{xyy}^{(2)}$  as an example for a brief analysis. Clearly, the absorptive part of  $\chi_{xyy}^{(2)}$  becomes nonzero only for photon energy larger than  $\sim 1.28$  eV (about half of the band gap) [see Table III and Fig. 5(a)]. In order to further analyze the prominent features in the calculated  $\chi^{(2)}(\omega)$  spectra of ML selenium, we plot the absolute values of the imaginary part  $\chi^{(2)}$  and compare the magnitude of the imaginary part of  $\chi^{(2)}(\omega)$  with the absorptive part of the dielectric function  $\varepsilon(\omega)$  (see Fig. 6).

Because of similar features, only four elements out of the eight nonzero elements of the second-order susceptibility tensor are presented in Fig. 6 for ML selenium. The SHG involves not only single-photon ( $\omega$ ) resonance but also double-photon ( $2\omega$ ) resonance. For  $\chi_{xyy}^{(2)}$ , Fig. 6(a) shows that the SHG spectra can be divided into two parts. The first part from 1.22 to 2.40 eV is primarily derived from double-photon resonances. On the other hand, the second part (above 2.40 eV) originates predominantly from single-photon resonances with some contribution from double-photon resonances [see Figs. 6(a) and (b)]. In the energy region, the spectra oscillate rapidly and decrease gradually at higher photon energies due to the

TABLE IV. Static dielectric constants ( $\varepsilon_x, \varepsilon_y$  and  $\varepsilon_z$ ), second-order susceptibility  $\chi_{xxx}^{(2)}(0)$  (pm/V),  $\chi_{xyy}^{(2)}(0)$  (pm/V),  $\chi_{xzz}^{(2)}(0)$  (pm/V),  $\chi_{xyx}^{(2)}(0)$  (pm/V),  $\chi_{yzy}^{(2)}(0)$  (pm/V),  $\chi_{zzy}^{(2)}(0)$  (pm/V) and  $\chi_{zxy}^{(2)}(0)$  (pm/V) as well as corresponding LEO coefficient of layered selenium calculated without (GGA) and with (SC) scissors correction.

	$\varepsilon_x$	$\varepsilon_y$	$\varepsilon_z$	$\chi_{xxx}^{(2)}$	$\chi_{xyy}^{(2)}$	$\chi_{xzz}^{(2)}$	$\chi_{xyx}^{(2)}$	$\chi_{yzy}^{(2)}$	$\chi_{zzy}^{(2)}$	$\chi_{zxy}^{(2)}$	$r_{xxx}$	$r_{xyy}$	$r_{xzz}$	$r_{xyz}$	$r_{yzx}$	$r_{yxy}$	$r_{zxx}$	$r_{zxy}$	
Bulk GGA	10.8 <sup>a</sup>		15.4 <sup>a</sup>	330 <sup>a</sup>		6 <sup>a</sup>					-5.63 <sup>a</sup>			-0.10 <sup>a</sup>					
SC	9.0 <sup>a</sup>		12.7 <sup>a</sup>	145 <sup>a</sup>		5 <sup>a</sup>					-3.58 <sup>a</sup>			-0.12 <sup>a</sup>					
ML GGA	13.7	9.6	5.6	96	311	5	78	86	78	9	61	-1.02	-4.72	-0.14	-1.18	-3.21	-1.18	-0.56	-1.60
SC	11.5	8.2	5.1	41	155	3	36	40	28	4	32	-0.63	-3.29	-0.10	-0.77	-1.92	-0.60	-0.29	-1.08
BL GGA	14.3	9.8	7.3	45	170	-20	60	67	37	-19	55	-0.45	-2.44	0.39	-0.86	-1.86	-0.53	0.72	-1.05
SC	11.9	8.2	6.4	17	92	-6	27	27	12	-11	25	-0.24	-1.87	0.15	-0.54	-1.01	-0.24	0.52	-0.65
TL GGA	14.5	9.8	8.1	39	133	-34	42	47	7	-33	38	-0.37	-1.87	0.59	-0.59	-1.17	-0.09	0.99	-0.64
SC	12.0	8.3	7.0	12	75	-11	18	19	1	-16	16	-0.17	-1.51	0.25	-0.37	-0.65	-0.03	0.64	-0.37

<sup>a</sup>Calculated value from reference 8.

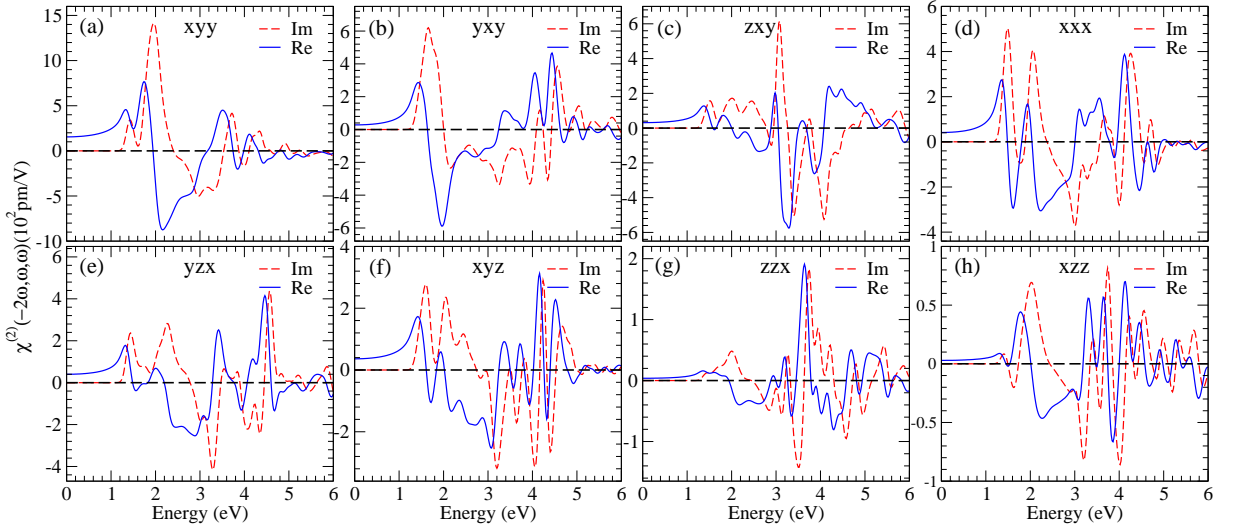


FIG. 5. Real and imaginary parts of eight independent nonzero second-order susceptibility for ML selenium.

coexistence of one and two-photon resonances. Remarkably, for the spectrum of  $|\chi_{xyy}^{(2)}|$ , the first prominent peak ranging from 1.20 to 2.0 eV corresponds to the significant peak in the  $\varepsilon_{bb}''(\omega/2)$  [see Figs. 6(c) and 6(d)], suggesting that it steps from two-photon resonances. It is clear from Fig. 6(d) that the peaks, above the absorption edge of  $\varepsilon_{bb}''(\omega)$ , may be related to the spectra in the  $\varepsilon_{bb}''(\omega/2)$  and  $\varepsilon_{bb}''(\omega)$ , indicating that they can be caused by both double-photon and single photon resonances. As for  $\chi_{zzx}^{(2)}$  and  $\chi_{xzz}^{(2)}$ , Figs. 6(e) and 6(g) show that the peaks from the absorption edge of  $\varepsilon_{cc}''(\omega/2)$  to the absorption edge of  $\varepsilon_{cc}''(\omega)$  in the  $|\text{Im}[\chi^{(2)}(\omega)]|$  spectra may be attributed to the two-photon resonances with  $E \parallel c$  [cf.  $\varepsilon_{cc}''(\omega/2)$ ]. In the higher photon energies, above the absorption edge of  $\varepsilon_{cc}''(\omega)$ , the spectra of the absolute values of the imaginary part  $\chi^{(2)}(\omega)$  oscillate rapidly. This is consistent with the fact that the energy region comes mainly from two-photon resonances with some contribution from one-photon resonances. Clearly, the magnitude of modulus of the imaginary parts  $\chi_{xyy}^{(2)}$  is larger than that of  $\chi_{xyx}^{(2)}$  and

much larger than that of  $\chi_{zzx}^{(2)}$  and  $\chi_{xzz}^{(2)}$ . The conclusion is further supported by the magnitude relationship of  $\varepsilon_{aa}''(\omega)$ ,  $\varepsilon_{bb}''(\omega)$  and  $\varepsilon_{cc}''(\omega)$  [or  $\varepsilon_{aa}''(\omega/2)$ ,  $\varepsilon_{bb}''(\omega/2)$  and  $\varepsilon_{cc}''(\omega/2)$ ]. It is noted that the magnitude of the absolute value of second-order NLO susceptibility  $\chi_{xyy}^{(2)}$  is around 1423 pm/V at 1.98 eV, which is nearly 2 times larger than that bulk counterpart and exceeds 6 times larger than that of GaN [6, 7], a widely used nonlinear optical semiconductor.

## B. Layered Te

It is worth noting that multilayer Te exhibit large static SHG coefficient, especially  $\chi_{xyy}^{(2)}(0)$  for BL Te (see Table V), being more than 100 times larger than that of GaN in both zinc-blende and wurtzite [6, 7]. Furthermore, BL Te exceeds 5 times higher static LEO coefficient ( $r_{yzx}$ ) than bulk GaN polytypes [6, 7]. Our calculations indicate that the 2D layered Te may have potential applications in

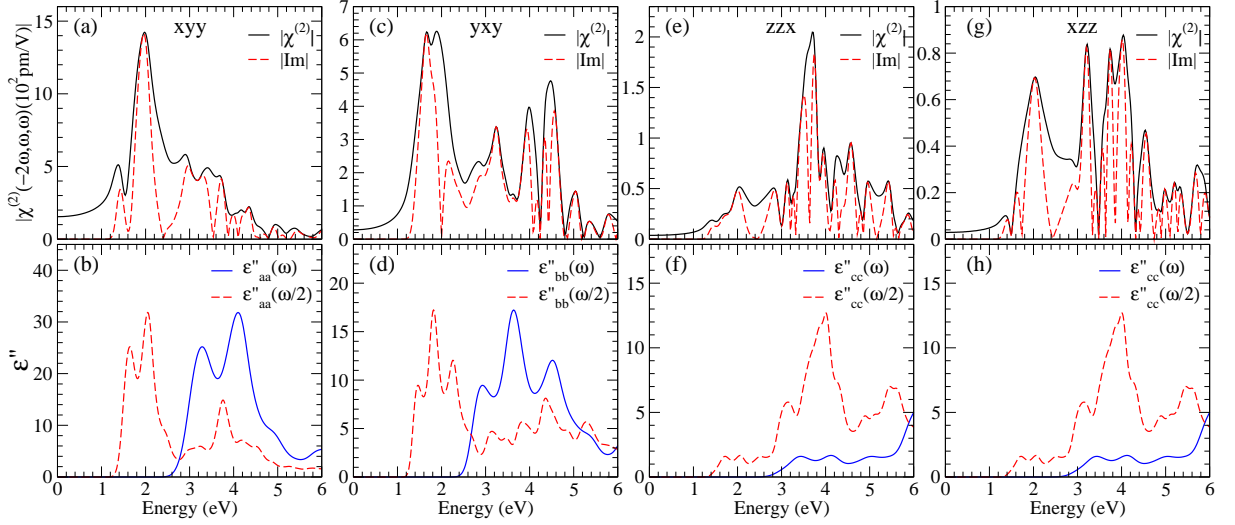


FIG. 6. Absolute value of the second-order susceptibility (a)  $\chi_{xy}^{(2)}$ , (c)  $\chi_{yx}^{(2)}$ , (e)  $\chi_{zzx}^{(2)}$  and (g)  $\chi_{xzz}^{(2)}$  for ML selenium. Imaginary part  $\varepsilon''(\omega)$  of the dielectric function for light polarization (b) and (d) perpendicular as well as (f) and (h) parallel to the  $c$  axis, respectively.

TABLE V. Static dielectric constants ( $\varepsilon_x, \varepsilon_y$  and  $\varepsilon_z$ ), second-order susceptibility  $\chi_{xxx}^{(2)}(0)$  (pm/V),  $\chi_{yyy}^{(2)}(0)$  (pm/V),  $\chi_{zzz}^{(2)}(0)$  (pm/V),  $\chi_{xyx}^{(2)}(0)$  (pm/V),  $\chi_{yxy}^{(2)}(0)$  (pm/V),  $\chi_{zxx}^{(2)}(0)$  (pm/V) and  $\chi_{zxy}^{(2)}(0)$  (pm/V) as well as corresponding LEO coefficient of layered tellurium calculated without (GGA) and with (SC) scissors correction.

	$\varepsilon_x$	$\varepsilon_y$	$\varepsilon_z$	$\chi_{xxx}^{(2)}$	$\chi_{yyy}^{(2)}$	$\chi_{zzz}^{(2)}$	$\chi_{xyx}^{(2)}$	$\chi_{yxy}^{(2)}$	$\chi_{zxx}^{(2)}$	$\chi_{zxy}^{(2)}$	$r_{xxx}$	$r_{xyy}$	$r_{xzz}$	$r_{xyz}$	$r_{yza}$	$r_{yxy}$	$r_{zxx}$	$r_{zxy}$	
Bulk GGA	40.6 <sup>a</sup>		57.2 <sup>a</sup>																
SC	33.2 <sup>a</sup>		49.0 <sup>a</sup>	169 <sup>a</sup>							-0.30 <sup>a</sup>								
BL GGA	36.5	33.7	14.4	1117	1963	54	1052	1050	1747	45	1034	-1.68	-3.19	-0.21	-1.71	-4.34	-2.84	-0.44	-3.94
SC	31.6	29.0	13.2	557	1077	31	592	585	897	0	591	-1.11	-2.34	-0.15	-1.29	-3.06	-1.95	0	-2.84
TL GGA	41.6	33.9	18.8	1903	1723	55	1245	1283	1468	46	1243	-2.20	-2.45	-0.14	-1.77	-4.02	-2.09	-0.26	-3.17
SC	35.3	28.8	16.8	823	872	18	656	644	683	-11	626	-1.32	-1.72	-0.06	-1.29	-2.67	-1.34	0.08	-2.11

<sup>a</sup>Calculated value from reference 8.

second-order nonlinear optical devices and linear electro-optic modulators. Obviously, the existence of interlayer and interchain interaction is further testified by the fact that static dielectric constants  $\varepsilon_y$  are similar for different layer structures, while  $\varepsilon_x$  and  $\varepsilon_z$  (light polarization along the chain and parallel to the direction of layers) is prominently diverse. In addition, the calculated real and imaginary parts of the second-order NLO susceptibility are displayed in Fig. 7 for TL and in Fig. S4 for BL in the SM. Obviously, the spectral shape of real and imaginary parts of  $\chi^{(2)}(\omega)$  are extremely similar for BL and TL tellurium, indicating the weak interlayer interaction in layered tellurium. Unlike layered selenium, the magnitude of second-order susceptibility for layered tellurium becomes larger and larger as the number of layers increases. For a specific semiconductor, the smaller the band gap and volume, the larger the magnitude of the second-order NLO susceptibility, as will be explained detailedly below. Therefore, this is not surprising that nonzero elements of TL tellurium  $\chi^{(2)}(\omega)$  are not much

larger than that of BL tellurium due to smaller band gap but with larger volume.

Due to similar features, only second-order NLO susceptibility  $\chi_{xxx}^{(2)}$ , largest nonzero element among all non-vanishing second harmonic generation (SHG) coefficient, is discussed in detail below. It is clear from Fig. 7(a) that second-order NLO susceptibility  $\chi_{xxx}^{(2)}$  is prominent in the optical photon energy range from  $\sim 0.44$  eV to  $\sim 1.86$  eV. In addition, in the energy range from 0 to 0.22 eV, the real part of the  $\chi_{xxx}^{(2)}$  remains almost constant, then increases steadily with the photon energy, and finally produces a small peak at  $\sim 0.58$  eV [see Fig. 7(a)]. In the energy region of 0.70-1.02 eV, the spectrum of  $\chi_{xxx}^{(2)}$  becomes negative and forms a pronounced peak at  $\sim 0.86$  eV. Beyond 1.02 eV, it becomes positive again and decreases gradually in the higher energy region. Interestingly, in spite of different positions and magnitude of peaks, the spectral tendency of the imaginary part of  $\chi^{(2)}(\omega)$  is rather similar to that of real part for all nonvanishing elements. Furthermore, the imaginary (absorp-

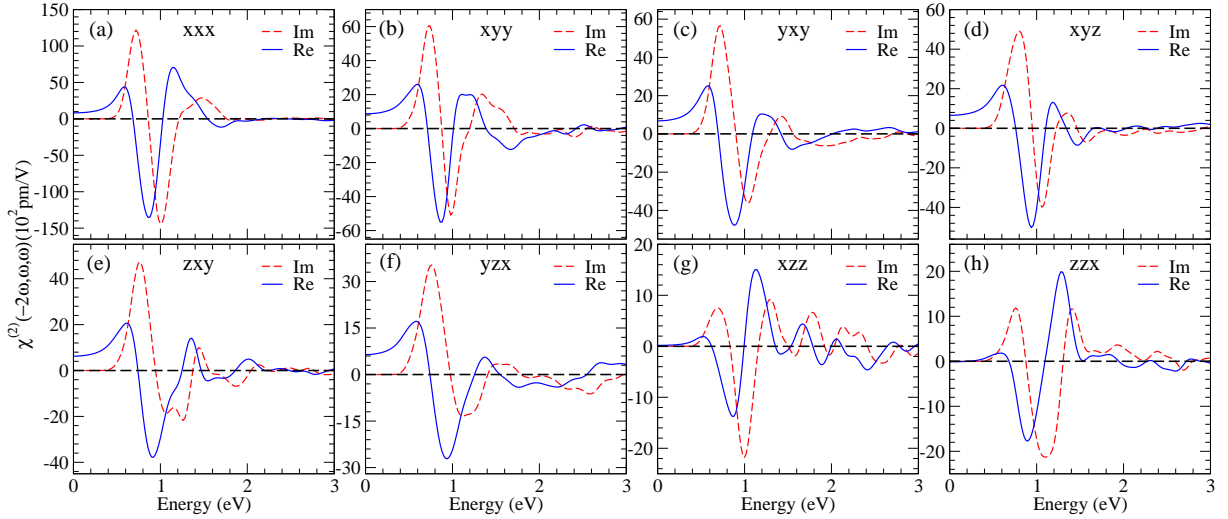


FIG. 7. Real and imaginary parts of eight independent nonzero second-order susceptibility for TL tellurium.

tive) part of  $\chi_{xxx}^{(2)}$  is nonzero only above  $\sim 0.24$  eV and exhibits an extremely huge peak around 1.0 eV [ Fig. 7(a)].

Likewise, to understand the features in the calculated second-order susceptibility spectra, the absolute values of the imaginary part  $\chi''^{(2)}(\omega)$  are plotted and compared with the imaginary part (absorptive part) of the dielectric function. Overall, the features of  $\chi^{(2)}(\omega)$  spectra are rather similar. Hence, in what follows, we take  $\chi_{xxx}^{(2)}$ ,  $\chi_{xyy}^{(2)}$ ,  $\chi_{xzz}^{(2)}$  and  $\chi_{zzx}^{(2)}$  of TL tellurium as example and analyze them in detail (see Fig. 8). Similarly, Fig. 8 suggests that the spectral feature of both  $\chi_{xzz}^{(2)}$  and  $\chi_{zzx}^{(2)}$  between  $\sim 0.44$  and  $\sim 1.72$  eV could be attributed to the two-photon resonances for  $\varepsilon''_{cc}(\omega/2)$ , while, in contrast, the rest structure (above  $\sim 1.72$  eV) stems from both single-photon ( $\omega$ ) [ $\varepsilon''_{cc}(\omega)$ ] and two-photon resonances [ $\varepsilon''_{cc}(\omega/2)$ ]. As a result, the SHG spectra, especially for  $\chi_{xzz}^{(2)}$ , oscillate rapidly and disappear gradually in the higher energy range [see Figs. 8(e) and 8(g)]. Note that the SHG coefficient of  $\chi_{xzz}^{(2)}$  and  $\chi_{zzx}^{(2)}$  are comparable to that of bulk Te, indicating their potential applications in NLO optical devices. Similarly, for  $\chi_{xxx}^{(2)}$  and  $\chi_{xyy}^{(2)}$ , the spectral structures between  $\sim 0.34$  eV and  $\sim 1.36$  eV are mainly due to double-photon ( $2\omega$ ) resonances for E||a and E||b [i.e.,  $\varepsilon''_{aa}(\omega/2)$  and  $\varepsilon''_{bb}(\omega/2)$ ], respectively. The second feature in the photon energies above 1.36 eV is mainly attributed to the single-photon resonances from  $\varepsilon''_{aa}(\omega)$  and  $\varepsilon''_{bb}(\omega)$ , respectively. Clearly, the magnitude of  $\chi_{xxx}^{(2)}$  is the largest and in general about several times larger than that of the other nonzero elements (see Fig. 7). This conclusion is further supported by the fact that the magnitude of  $\varepsilon''_{aa}(\omega)$  [ $\varepsilon''_{aa}(\omega/2)$ ] is larger than that of  $\varepsilon''_{bb}(\omega)$  [ $\varepsilon''_{bb}(\omega/2)$ ], and much larger than  $\varepsilon''_{cc}(\omega)$  [ $\varepsilon''_{cc}(\omega/2)$ ]. Excitingly, the magnitude of  $|\chi_{xxx}^{(2)}(-2\omega, \omega, \omega)|$  is as high as 15005 pm/V at 0.98 eV, which surpasses 4 times

larger than that of bulk Te [8] and 65 times larger than that of GaN [6, 7]. Overall, the calculations of second-order NLO susceptibility suggest that few-layer tellurium possess promising applications in, e.g., optical switching, ultrathin second-harmonic and sum frequency generation devices, optical modulation, and light signal modulators, and so on.

## VI. BULK PHOTOVOLTAIC EFFECT

### A. Layered Se

The generation of photocurrent is a crucial component for solar energy harvesting progress and could be divided into two steps. Firstly, light irradiation produce electron-hole pairs, and then electrons and holes separate in space. It is all known that the latter progress is significantly different for traditional photovoltaic effect and the bulk photovoltaic effect (BPVE). In conventional solar cells [see Fig. 9(a)], the built-in electric field from the interface of p-n junctions would separate the photoexcited electrons and holes. Therefore, conventional photovoltaic effect requires high carrier mobility, long carrier lifetime and favorable interface control, which brings challenges to the development of excellent photovoltaic materials. Whereas, the bulk photovoltaic effect (BPVE) can be observed in single-phase homogeneous materials with broken inversion symmetry. With no need for interface, electrons in the BPVE are continuously excited to quasiparticle coherent states with inherent momentum. As shown in the simplified picture [Fig. 9(b)], the photoexcited nonthermalized carriers in the conduction band shift from the top to the bottom of the band and bring about the shift  $l_0$  in space. In consequence, the spontaneous shift current comes into being in the crystals with

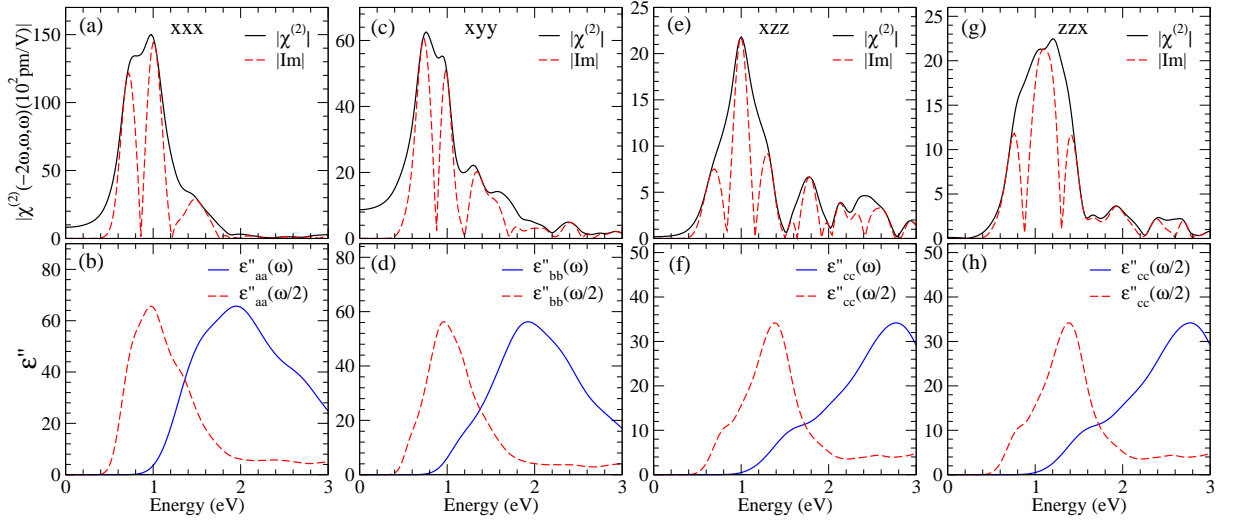


FIG. 8. Absolute value of the second-order susceptibility (a)  $\chi_{xxx}^{(2)}$ , (c)  $\chi_{xyy}^{(2)}$ , (e)  $\chi_{xzz}^{(2)}$  and (g)  $\chi_{zzx}^{(2)}$  for TL tellurium. Imaginary part  $\varepsilon''(\omega)$  of the dielectric function for light polarization (b) and (d) perpendicular as well as (f) and (h) parallel to the  $c$  axis, respectively.

symmetry breaking.

On the basis of specific symmetry class, the calculated SHC coefficients share uniform nonzero elements with that of second-order NLO susceptibility, i.e.  $\sigma_{xxx}$ ,  $\sigma_{yxy}$ ,  $\sigma_{xyy}$ ,  $\sigma_{zxy}$ ,  $\sigma_{xyz}$ ,  $\sigma_{yzx}$ ,  $\sigma_{zxx}$  and  $\sigma_{zzz}$ . However, the fact that the direction of light polarization parallel ( $E \parallel c$ ) to the  $c$  axis will be no shift current since  $c$ -axis is the out-of-plane direction. Therefore, in this paper, we do not display shift-current spectrum of  $\sigma_{zxx}$  and  $\sigma_{zxy}$ . As depicted in Fig. 10 and Fig. S5, compared with SHG coefficients, the shift-current spectra exhibit significantly disparate characteristic for different layered selenium, especially for monolayer Se, indicating the stronger structure dependence and a more significant role of weak vdW interactions. Figs. 10 and S5 show clearly that  $\sigma_{xxx}$  is the maximal element of shift current responses for BL and TL Se and  $\sigma_{yxy}$  is the corresponding maximum for ML Se. Even so, for different layered Se, the general tendency of SHC spectra is similar. In what follows, we take  $\sigma_{xxx}$  as an example to carry out detailed analysis. As depicted in Fig. 10(a), the threshold of shift current spectra is corresponding to the absorption edge of the imaginary part of the dielectric function  $\varepsilon(\omega)$ . For TL Se, the shift current responses  $\sigma_{yxy}$  exhibit a peak at  $\sim 2.72$  eV in the visible frequency range, while the element  $\sigma_{xxx}$  of ML and  $\sigma_{xyz}$  of BL possess a slightly small peak, respectively centered at  $\sim 2.96$  eV and  $\sim 2.50$  eV. Beyond the visible spectrum (at 3.40-5.92 eV), ML Se shows an enhanced peak and the magnitude is comparable to the maximum response obtained from BaTiO<sub>3</sub> [18], an archetypical single-crystal with the bulk photovoltaic effect (BPVE). In range of high energy, BL and TL Se share more similar spectral structures, while ML Se exhibits slightly larger peak in the spectral of  $\sigma_{xxx}$  centered at  $\sim 7.68$  eV. Overall, our results prove that 2D layered Se

are excellent broadband nonlinear material and possess potential application prospects in the nonlinear optics field, particularly in the ultraviolet regions.

Photoresponsivity and Glass coefficient are other two important quantities of bulk photovoltaic effect (BPVE) which give the direct interpretation with the experimental measurements. The calculated photoresponsivity for 2D layered Se systems are displayed in Fig. 11 and Fig. S6. Similar to shift current responses, the photoresponsivity spectra of BL and TL Se are roughly identical. As clearly demonstrated in Fig. 11, for ML Se, the photoresponsivity element  $K_{yxy}$  exhibits the maximum 47.4 mA/W and exceeds 9 times larger than that in few-layer black Phosphorus [79]. However, for BL and TL Se, the maximum is obtained from  $K_{xxx}$ . Furthermore, the maximum value of photoresponsivity in BL Se is negative, which turns positive when the thickness increases to three layer. This unusual photoresponsivity will contribute to the comprehensive exploration of two-dimensional layered materials with particular properties. In particular, the value of the photoresponsivity could be further drastically enhanced by engineering a detector based on different combinations of the heterostructure [79–83]. Notably, the photoresponsivity  $K$  based on layered Se are located in a wide energy range from  $\sim 2$  eV to  $\sim 12$  eV and mainly situated at the ultraviolet region for all structures. These findings not only enhance our knowledge on optical properties of 2D layered Se, but also provide a foundation to the further development of optoelectronic devices.

In the present work, we have calculated three components of Glass coefficient for each 2D layered Se. As clearly demonstrated in Fig. 12, the spectral shape of Glass coefficient  $G_{xxx}$  for different layers of selenium tend to be similar. Prominently, the calculated maximum

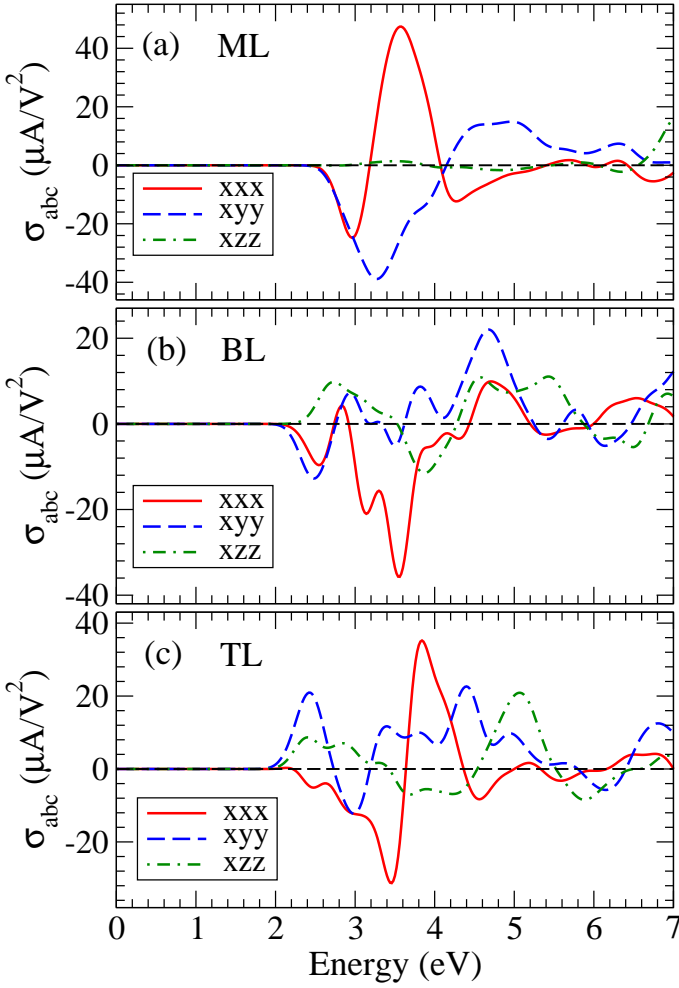


FIG. 9. (a) The conventional photovoltaic effect and (b) bulk photovoltaic effect (BPVE).

value of Glass coefficient for BL Se in the visible range is comparable to that of single-layer monochalcogenides [22] and exceeds the maximum response observed for BaTiO<sub>3</sub> thin film by 8 times [84]. As the number of the layers decreases from two to single-layer limit, the maximum response experiences a blueshift, slightly weaker than that obtained in BL Se [see Figs. 12(a) and 12(b)]. Whereas, when the thickness increases to three layers, the Glass coefficient  $G_{xxx}$  decreased dramatically and the maximum value is much weaker than that of ML and BL Se. There is, in addition, the maximum in  $G_{xzz}$  not in  $G_{xxx}$  for TL Se. Overall, the Glass coefficients are tunable with the number of layers due to interlayer van der Waals interaction.

### B. Layered Te

Fig. 13 and S7 display the shift current as a function of light frequency for BL and TL Te. Clearly, our calcula-

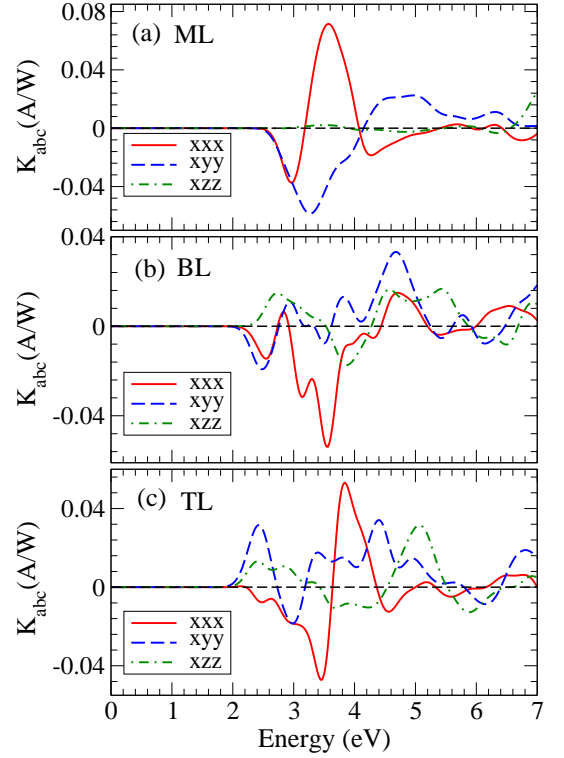


FIG. 10. The shift current response ( $\sigma$ ) versus the photon energy for ML, BL and TL selenium.

tions predict that both materials exhibit enormous shift current response. Especially for TL Te, the magnitude of shift current  $\sigma_{xxx}$  at 1.66 eV (visible range) exceeds the maximum of the photovoltaic responses observed for single-layer GeS by 2 times [22]. As for BL Te,  $\sigma_{yzz}$  is the maximal shift current element being up to  $\sim 126 \mu\text{A}/\text{V}^2$ , which is comparable to single-layer Ge and Sn monochalcogenides [22]. To our knowledge, the shift current response of the single-layer Ge and Sn monochalcogenides is larger than that of any one previously obtained in polar systems. Compared to layered Se, the shift current spectra of BL and TL Te distribute in much smaller energy range (about 1.0-4.5 eV). Or rather, as described in Fig.13 and S7, dominating shift-current response occurs in the visible spectrum (1.64-3.19 eV), and thus prominent BPVE in few-layer Te could be excited by visible light. All in all, our calculations indicate that two-dimensional tellurium possesses potential applications in photovoltaic devices and would boost further research on the experiments. Such giant SHC response can be attributed to narrow band gap and high covalent bond, which will be explained below in detail.

In Fig. 14 and S8, we exhibit our calculated photoresponsivity of layered Te materials researched in this work. The research of photoresponsivity for materials with reduced dimensionality is of great significance for further development of excellent photodetectors in the future. Moreover, much larger photoresponsivity is favorable to

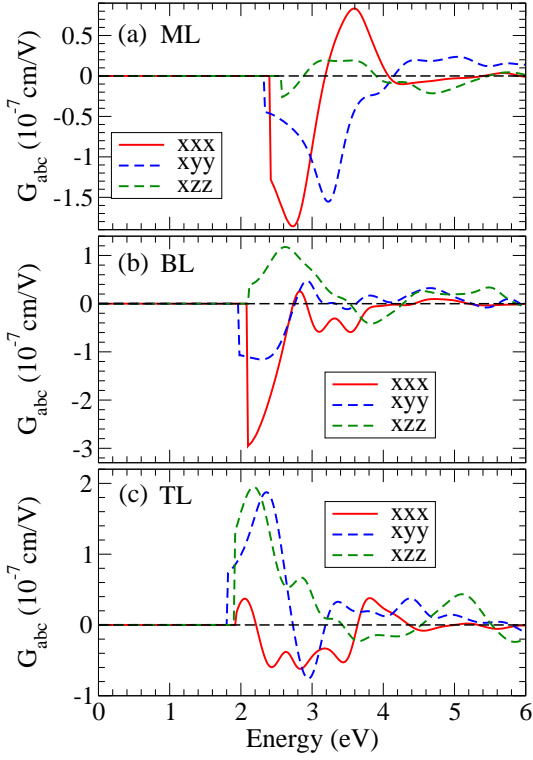


FIG. 11. The calculated photoresponsivity  $K$  versus the photon energy for ML, BL and TL selenium.

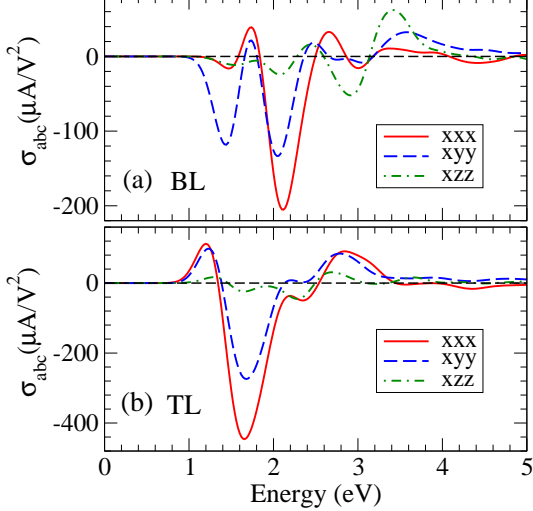


FIG. 12. The calculated Glass coefficients  $G$  versus the photon energy for ML, BL and TL selenium.

improve the performance of optical and nanoelectronics devices. As expected, few-layer Te, particularly for TL Te, exhibit large photoresponsivity, much stronger than that studied in the known noncentrosymmetric materials, such as  $\text{NaAsSe}_2$  ( $0.1 \mu\text{A/W}$ ) [20],  $\text{BiFeO}_3$  ( $0.1 \mu\text{A/W}$ ) [85], hybrid perovskites ( $1 \mu\text{A/W}$ ) [86] and  $\text{BaTiO}_3$  ( $10$

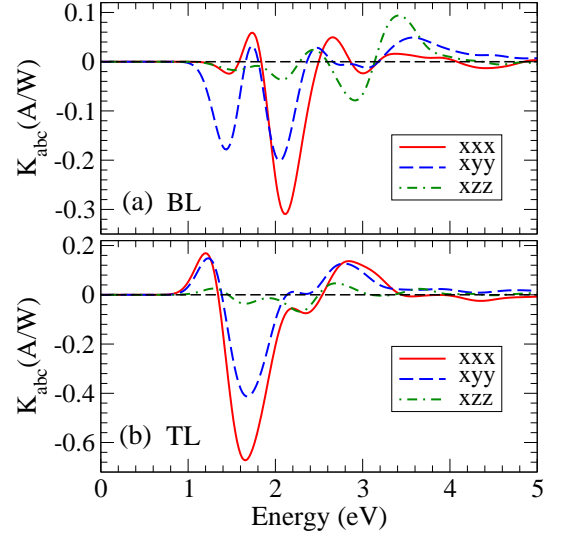


FIG. 13. The shift current response ( $\sigma$ ) versus the photon energy for BL and TL tellurium.

$\mu\text{A/W}$ ) [18]. Strikingly, the strong photoresponsivity of layered Te are distributed in the whole visible range and the maximum for BL and TL Te are 2 times and 3 times greater than that of GeS [70], respectively. The characteristic of low dimensionality and narrow band gap make few-layer Te obtain enhanced intrinsic photovoltaic effect and also improve the efficiency of converting solar into electric energy. Therefore, our work not only demonstrate that it is possible to realize the enhanced efficiency of photovoltaic effect (BPVE) by materials with broken inversion symmetry not traditional p-n junctions, but also expand the family of nanoelectronics devices.

As demonstrated by previous work, favorable covalent bonding and delocalized electronic states are to the benefit of enhanced shift current effects. When the samples is thick enough to absorb all incident light, the Glass coefficient is used to describe the principal mechanism of BPVE, namely shift current. In order to display clearly the relationship between the Glass coefficient and the light frequency, we calculated three Glass coefficient elements plotted in Fig.15. The maximal Glass coefficient in BL Te can exceed the chalcogenide compounds [20] or  $\text{BaTiO}_3$  [84] thin film by an order of magnitude larger and even is up to 4 times greater than that of single-layer monochalcogenides [22]. Prominently, we find that TL Te exhibits colossal Glass coefficient  $G_{xxx}$  exceeding  $10 \times 10^{-7} \text{cm/V}$ , the largest Glass coefficient obtained so far. Additionally, we also found that the dominating spectra of Glass coefficient for layered Te lie in the infrared range, indicating that few-layer Te would be an excellent candidate for state of the art infrared detectors and high-performance nanoelectronics devices.

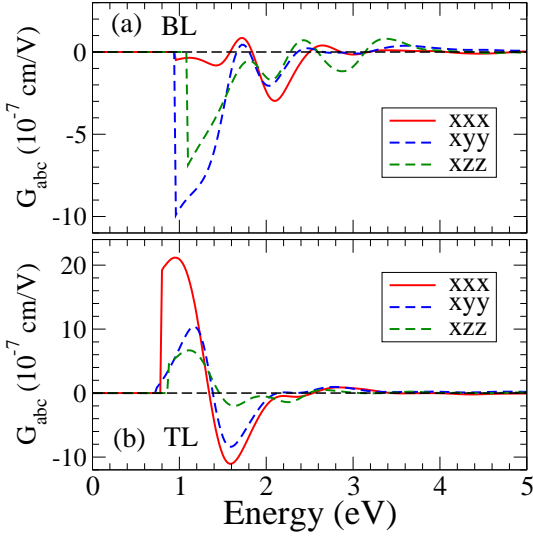


FIG. 14. The calculated photoresponsivity  $K$  versus the photon energy for BL and TL tellurium.

## VII. DEFORMATION CHARGE DENSITY

For a particular semiconductor, the imaginary part of the dielectric function and second-order NLO susceptibility are significantly affected by the band gap. This could be explained by the fact that the energy differences between the initial and final states of optical excitations are in the denominators of Eqs. (1), (4), and (5), indicating that the smaller the band gap is, the larger the magnitude of optical response would be. Particularly for the imaginary part of the SHG coefficients, the magnitude, especially in the low energy, would be roughly proportional to the inverse of the fourth power of the band gap. The magnitude of shift current photovoltaic effect, as has been previously proved [18], depends powerfully on the electronic structure, including band gap and covalency. As a result, for identical layered Se and Te, in spite of similar crystalline and electronic structures, the calculated magnitude of the imaginary part of the dielectric function, SHG coefficients and bulk photovoltaic effect for tellurium are much larger than that of selenium due to smaller band gap. Interestingly, the band gap of few-layer Te is larger than the optical frequencies of interest, showing that the materials would be useful for the NLO applications. Therefore, to search for NLO materials with large NLO response, one could focus on those semiconductors with smallest possible band gaps which are larger than the optical frequencies required by specific NLO applications.

Compared to other semiconductors with similar band gaps, layered Se or Te exhibit much larger NLO effects. Therefore, to further investigate the origins of the enhanced NLO responses of 2D selenium and tellurium, we also calculate the difference charge density which is defined as the difference between the valence charge den-

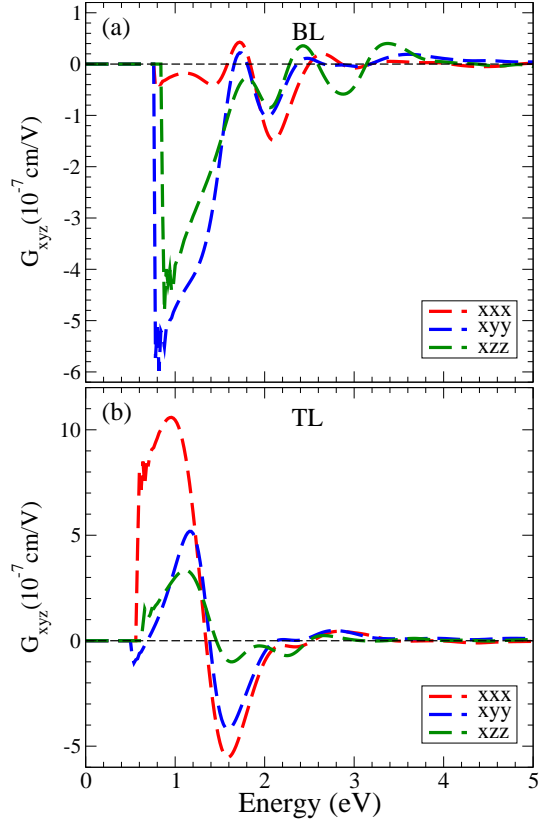


FIG. 15. The calculated Glass coefficients  $G$  versus the photon energy for BL and TL tellurium.

sity and the superposition of the free atomic charge densities, as plotted in Fig. 16. From bulk counterparts [8] to different layered structures, there is no significant changes for the difference charge density, indicating that these materials possess rather similar charge movement and directions of bonding polarization. Indeed, a considerable electron charges accumulate in the vicinity of the Se-Se (Te-Te) bond center by using up the charge around the atoms along the bond directions. As a consequence, strong directional covalent bond come into being (see Fig. 16). It is noted that strong covalent bond would generate large spatial overlap between the wave functions of initial and final states and thus form large optical matrix elements, and then enhanced NLO responses are produced. Furthermore, Fig. 16 also clearly displays a charge buildup around each atom in the direction perpendicular to the chain, manifesting the existence of lone-pair electrons which is also significant origin of enhanced NLO effect. This could be explained by the fact that the presence of lone-pair electrons is beneficial to the generation of induced dipole oscillations by the optical electric fields, thus leading to large  $\chi^{(2)}$  values [87, 88]. Therefore, in general, quasi one-dimensional crystals with strong directional covalency and lone-pair electrons would possess large NLO values. Moreover, High anisotropy would result in large joint DOS, and

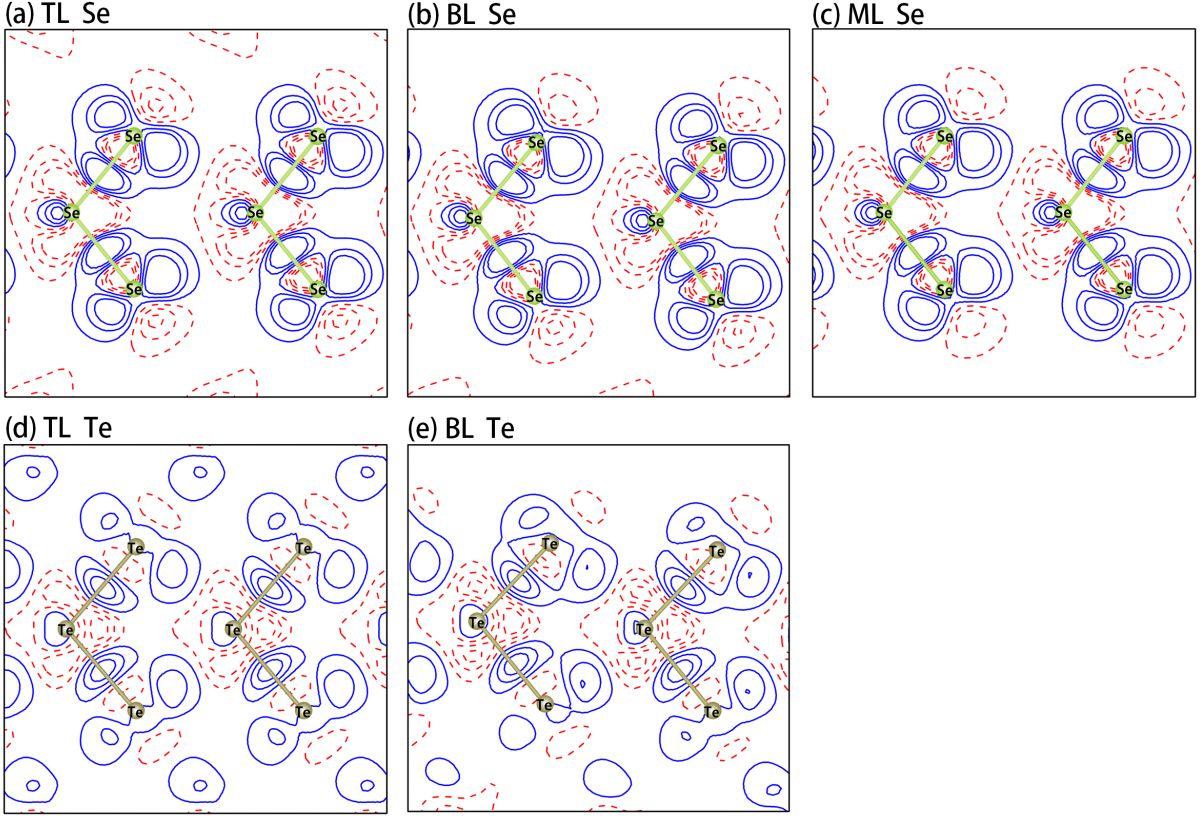


FIG. 16. The contour plots of the deformation charge densities for (a),(b) and (c) corresponding to TL, BL and ML selenium, as well as (d) and (e) corresponding to TL and BL tellurium. The contour interval is  $0.02 e/\text{\AA}^3$ . The electron accumulation is depicted by positive contours (blue solid lines), while the electron depletion is represented by negative contours (red dashed lines)

then give rise to large BPV and SHG effect [89, 90]. Note that the volume, as mentioned above, would also exert remarkable effects on linear and nonlinear optical responses. As shown in Eqs. (1), (4), and (5), the smaller the volume, the larger the magnitude of the imaginary part of the dielectric function and second-order NLO susceptibility. In consequence, the fact, that the magnitude of second-order NLO effect of monolayer Se are larger than that of bilayer and thilayer Se, may be explained as the reason of higher anisotropy and smaller volume. Conversely, bilayer Te is slightly smaller than that of thilayer Te. It might be because thilayer Te possesses smaller band gap in spite of lower anisotropy and larger volume. In general, to design good NLO materials, practical strategies are to search for materials with smallest possible band gaps, high anisotropy, strong covalency and/or lone-pair electrons in low dimensional systems.

## VIII. CONCLUSION

We have carried out a systematic first-principles calculation of the linear and nonlinear optical properties of layered selenium and tellurium within density-functional theory in the generalized gradient approximation. In order to adequately consider many-body effects, especially quasiparticle self-energy correction, we perform the scissors correction (SC) in the optical calculations. The energy of scissors correction is defined as the band gap differences between the hybrid HSE functional with the SOC include calculations and GGA calculations. Excitingly, we find that all 2D layered materials possess large NLO responses, especially in trilayer Te, which exhibits enormous second-harmonic generation coefficient  $\chi_{xxx}^{(2)}$  being more than 65 times larger than that of GaN and even more than 4 times than corresponding bulk. In particular, we find that the magnitude of  $\varepsilon''_{aa}(\omega)$  [ $\varepsilon''_{aa}(\omega/2)$ ] is larger than that of  $\varepsilon''_{bb}(\omega)$  [ $\varepsilon''_{bb}(\omega/2)$ ], and much larger than  $\varepsilon''_{cc}(\omega)$  [ $\varepsilon''_{cc}(\omega/2)$ ]. Accordingly,  $\chi_{xxx}^{(2)}$  is the largest SHG coefficient, the magnitude of the absolute value is as high as 15005 pm/V. The same phenomenon is

found in monolayer and few-layer Se. Compared to most semiconductors, ML Se also displays prominent NLO effect with maximal nonvanishing SHG coefficient  $\chi_{xyy}^{(2)}$  being as large as 1423 pm/V, which is nearly 2 times greater than that of bulk counterpart and exceeds 6 times larger than that of GaN. Remarkably, BL Te exhibits gigantic static SHG coefficient  $\chi_{xyy}^{(2)}$ , which is more than 100 times larger than that of GaN in both zinc-blende and wurtzite. Furthermore, ML Se and BL Te severally have huge linear electro-optic coefficients  $r_{xyy}$  and  $r_{yzx}$ , being up to 6 times and 5 times larger than that of bulk GaN polytypes, respectively. Another interesting discovery is that narrow band gap can increase the BPVE and SHG response more significantly for multilayer Te. Since small bandgap favors the large NLO response while the relatively large volume suppresses NLO response. In fact, TL Te exhibits stronger BPVE and SHG responses than that of BL Te. Additionally, we find that the maximum of the shift current in the visible range for TL Te is more than that of ML GeS by 2 times. In short, layered selenium and tellurium are promising NLO materials for applications in, e.g., photovoltaic devices, second-harmonic generation, sum frequency generation, frequency conversion, phase matching, electro-optical switches and light signal modulators. The remarkable features in the spectra of  $\chi''^{(2)}(-2\omega, \omega, \omega)$  of

these 2D layered Se and Te could be correlated with the peaks in the imaginary part of the corresponding optical dielectric function in terms of single-photon and double-photon resonances. Finally, compared with the semiconductors with similar band gaps, the enhanced BPV effect, SHG and LEO coefficients in 2D layered selenium and tellurium could be interpreted as the results of their two-dimensional, or rather quasi-one-dimensional structures with high anisotropy, directional covalent bonding and lone-pair electrons. We hope that our work will stimulate further experiments on the second-order nonlinear optical responses in these fascinating 2D layered elemental material.

## ACKNOWLEDGEMENTS

M. C. thanks Department of Physics and Center for Theoretical Physics, National Taiwan University for its hospitality during her three months visit. Work at Xiamen University is supported by the National Key R&D Program of China (Grant No. 2016YFA0202601), and the National Natural Science Foundation of China (No. 11574257). G. Y. G. acknowledges support from the Ministry of Science and Technology, the Academia Sinica, the National Center for Theoretical Sciences in Taiwan.

- 
- [1] Y. R. Shen, *The Principle of Nonlinear Optics* (John Wiley and Sons Inc., New Jersey, 2003).
- [2] R. W. Boyd, *Nonlinear Optics* (Elsevier Science, Amsterdam, 2003).
- [3] R. K. Chang, J. Ducuing, and N. Bloembergen, Dispersion of the Optical Nonlinearity in Semiconductors, *Phys. Rev. Lett.* **15**, 415 (1965).
- [4] H. Zhong, Z. H. Levine, D. C. Allan, and J. W. Wilkins, Band-theoretic calculation of the optical activity tensor of  $\alpha$ -quartz and trigonal Se, *Phys. Rev. B* **48**, 1384 (1993).
- [5] J. L. P. Hughes and J. E. Sipe, Calculation of second-order optical response in semiconductors, *Phys. Rev. B* **53**, 10751 (1996).
- [6] V. I. Gavrilenko and R. Q. Wu, Linear and nonlinear optical properties of group-III nitrides, *Phys. Rev. B* **61**, 2632 (2000).
- [7] D. J. Cai and G.-Y. Guo, Tuning linear and nonlinear optical properties of wurtzite GaN by  $c$ -axial stress, *J. Phys. D: Appl. Phys.* **42**, 185107 (2009).
- [8] M. J. Cheng, S. Q. Wu, Z.-Z. Zhu, and G.-Y. Guo, Large second-harmonic generation and linear electro-optic effect in trigonal selenium and tellurium, *Phys. Rev. B* **100**, 035202 (2019).
- [9] G. Y. Guo, K. C. Chu, D.-S. Wang, and C.-G. Duan, Linear and nonlinear optical properties of carbon nanotubes from first-principles calculations, *Phys. Rev. B* **69**, 205416 (2004).
- [10] G. Y. Guo and J. C. Lin, Second-harmonic generation and linear electro-optical coefficients of BN nanotubes, *Phys. Rev. B* **72**, 075416 (2005); Erratum: Second-harmonic generation and linear electro-optical coefficients of BN nanotubes [Phys. Rev. B **72**, 075416 (2005)], **77**, 049901 (2008).
- [11] C.-Y. Wang and G.-Y. Guo, Nonlinear optical properties of transition-metal dichalcogenide  $\text{MX}_2$  ( $\text{M} = \text{Mo}, \text{W}$ ;  $\text{X} = \text{S}, \text{Se}$ ) monolayers and trilayers from first-principles calculations, *J. Phys. Chem. C* **119**, 13268 (2015).
- [12] L. Hu, X. Huang, and D. Wei, Layer-independent and layer-dependent nonlinear optical properties of two-dimensional GaX ( $\text{X} = \text{S}, \text{Se}, \text{Te}$ ) nanosheets. *Phys. Chem. Chem. Phys.* **19**, 11131 (2017).
- [13] H. Wang and X. F. Qian, Giant optical second harmonic generation in two-dimensional multiferroics. *Nano Lett.* **17**, 5027 (2017).
- [14] S. R. Panday, and B. M. Fregoso, Strong second harmonic generation in two-dimensional ferroelectric IV-monochalcogenides, *J. Phys.: Condens. Matter* **29**, 43LT01 (2017); Corrigendum: Strong second harmonic generation in two-dimensional ferroelectric IV-monochalcogenides (2017 *J. Phys.: Condens. Matter* **29** 43LT01), **30**, 179501 (2018).
- [15] Q. Wu and X.-C. Zhang, Ultrafast electro-optic field sensors, *Appl. Phys. Lett.* **68**, 1604 (1996).
- [16] A. G. Chynoweth, Surface Space-Charge Layers in Barium Titanate, *Phys. Rev.* **102**, 705 (1956).
- [17] A. M. Glass, D. von der Linde, and T. J. Negran, High-voltage bulk photovoltaic effect and the photorefractive process in  $\text{LiNbO}_3$ , *Appl. Phys. Lett.* **25**, 233 (1974).
- [18] S. M. Young and A. M. Rappe, First Principles Calculation of the Shift Current Photovoltaic Effect in Ferroelectrics, *Phys. Rev. Lett.* **109**, 116601 (2012).

- [19] A. Bhatnagar, A. R. Chaudhuri, Y. H. Kim, D. Hesse, and M. Alexe, Role of domain walls in the abnormal photovoltaic effect in BiFeO<sub>3</sub>, *Nat. Commun.* **4**, 2835 (2013).
- [20] J. A. Brehm, S. M. Young, F. Zheng, and A. M. Rappe, First-principles calculation of the bulk photovoltaic effect in the polar compounds LiAsS<sub>2</sub>, LiAsSe<sub>2</sub>, and NaAsSe<sub>2</sub>, *J. Chem. Phys.* **141**, 204704 (2014).
- [21] L. Z. Tan and A. M. Rappe, Enhancement of the Bulk Photovoltaic Effect in Topological Insulators, *Phys. Rev. Lett.* **116**, 237402 (2016).
- [22] T. Rangel, B. M. Fregoso, B. S. Mendoza, T. Morimoto, J. E. Moore, and J. B. Neaton, Large Bulk Photovoltaic Effect and Spontaneous Polarization of Single-Layer Monochalcogenides, *Phys. Rev. Lett.* **119**, 067402 (2017).
- [23] S.-J. Gong, F. Zheng, and A. M. Rappe, Phonon Influence on Bulk Photovoltaic Effect in the Ferroelectric Semiconductor GeTe, *Phys. Rev. Lett.* **121**, 017402 (2018).
- [24] L. A. Agapito, N. Kioussis, W. A. Goddard III, and N. P. Ong, Novel Family of Chiral-Based Topological Insulators: Elemental Tellurium under Strain, *Phys. Rev. Lett.* **110**, 176401 (2013).
- [25] H. Peng, N. Kioussis, and G. J. Snyder, Elemental tellurium as a chiral p-type thermoelectric material, *Phys. Rev. B* **89**, 195206 (2014).
- [26] M. Hirayama, R. Okugawa, S. Ishibashi, S. Murakami, and T. Miyake, Weyl Node and Spin Texture in Trigonal Tellurium and Selenium, *Phys. Rev. Lett.* **114**, 206401 (2015).
- [27] C. Şahin, J. Rou, J. Ma, and D. A. Pesin, Pancharatnam-Berry phase and kinetic magnetoelectric effect in trigonal tellurium, *Phys. Rev. B* **97**, 205206 (2018).
- [28] S. S. Tsirkin, P. A. Puentes, and I. Souza, Gyrotropic effects in trigonal tellurium studied from first principles, *Phys. Rev. B* **97**, 035158 (2018).
- [29] H. O. H. Churchill, G. J. Salamo, S.-Q. Yu, T. Hironaka, X. Hu, J. Stacy, and I. Shih, Toward Single Atom Chains with Exfoliated Tellurium, *Nanoscale Res. Lett.* **12**, 488 (2017).
- [30] I. L. Li, J. P. Zhai, P. Launois, S. C. Ruan, and Z. K. Tang, Geometry, Phase Stability, and Electronic Properties of Isolated Selenium Chains Incorporated in a Nanoporous Matrix, *J. Am. Chem. Soc.* **127**, 16111 (2005).
- [31] D. J. Olechna and R. S. Knox, Energy-Band Structure of Selenium Chains, *Phys. Rev.* **140**, A986 (1965).
- [32] M. Springborg, and R. O. Jones, Sulfur and selenium helices: Structure and electronic properties, *J. Chem. Phys.* **88**, 2652 (1988).
- [33] P. Ghosh, M. U. Kahaly, and U. V. Waghmare, Atomic and electronic structures, elastic properties, and optical conductivity of bulk Te and Te nanowires: A first-principles study, *Phys. Rev. B* **75**, 245437 (2007).
- [34] M. U. Kahaly, P. Ghosh, S. Narasimhan, and U. V. Waghmare, Size dependence of structural, electronic, elastic, and optical properties of selenium nanowires: A first-principles study, *J. Chem. Phys.* **128**, 044718 (2008).
- [35] B. Tuttle, S. Alhassan, and S. Pantelides, Computational Predictions for Single Chain Chalcogenide-Based One-Dimensional Materials, *Nanomaterials (Basel)* **7**, 115 (2017).
- [36] E. Andharia, T. P. Kaloni, G. J. Salamo, S.-Q. Yu, H. O. H. Churchill, and S. Barraza-Lopez, Exfoliation energy, quasiparticle band structure, and excitonic properties of selenium and tellurium atomic chains, *Phys. Rev. B* **98**, 035420 (2018).
- [37] Y. Y. Pan, S. Y. Gao, L. Yang, and J. Lu, Dependence of excited-state properties of tellurium on dimensionality: From bulk to two dimensions to one dimensions, *Phys. Rev. B* **98**, 085135 (2018).
- [38] J. K. Qin, G. Qiu, J. Jian, H. Zhou, L. M. Yang, A. Charnas, D. Y. Zemlyanov, C.-Y. Xu, X. F. Xu, W. Z. Wu, H. Y. Wang, and P. D. Ye, Controlled Growth of a Large-Size 2D Selenium Nanosheet and Its Electronic and Optoelectronic Applications, *ACS Nano* **11**, 10222 (2017).
- [39] Z. L. Zhu, X. L. Cai, S. H. Yi, J. L. Chen, Y. W. Dai, C. Y. Niu, Z. X. Guo, M. H. Xie, F. Liu, J.-H. Cho, Y. Jia, and Z. Y. Zhang, Multivalency-Driven Formation of Te-Based Monolayer Materials: A Combined First-Principles and Experimental study, *Phys. Rev. Lett.* **119**, 106101 (2017).
- [40] L. Xian, A. P. Paz, E. Bianco, P. M. Ajayan, and A. Rubio, Square selenene and tellurene: novel group VI elemental 2D materials with nontrivial topological properties, *2D Mater.* **4**, 041003 (2017).
- [41] X.-X. Xue, Y.-X. Feng, L. Liao, Q.-J. Chen, D. Wang, L.-M. Tang, and K. Q. Chen, Strain tuning of electronic properties of various dimension elemental tellurium with broken screw symmetry, *J. Phys.: Condens. Matter* **30**, 125001 (2018).
- [42] S. Sharma, N. Singh, and U. Schwingenschlögl, Two-Dimensional Tellurene as Excellent Thermoelectric Material, *ACS Appl. Energy Mater.* **1**, 1950 (2018).
- [43] T. T. Debela and H. S. Kang, Phase polymorphism and electronic structures of TeSe<sub>2</sub>, *J. Mater. Chem. C* **6**, 10218 (2018).
- [44] W. Zhang, Q. S. Wu, O. V. Yazyev, H. M. Weng, Z. X. Guo, W.-D. Cheng, and G.-L. Chai, Topological phase transitions driven by strain in monolayer tellurium, *Phys. Rev. B* **98**, 115411 (2018).
- [45] Y. Chen, J. Y. Liu, J. B. Yu, Y. G. Guo, and Q. Sun, Symmetry-breaking induced large piezoelectricity in Janus tellurene materials, *Phys. Chem. Chem. Phys.* **21**, 1207 (2019).
- [46] G. Liu, Z. B. Gao, and J. Ren, Anisotropic thermal expansion and thermodynamic properties of monolayer  $\beta$ -Te, *Phys. Rev. B* **99**, 195436 (2019).
- [47] J. L. Chen, Y. W. Dai, Y. Q. Ma, X. Q. Dai, W. K. Ho, and M. H. Xie, Ultrathin  $\beta$ -tellurium layers grown on highly oriented pyrolytic graphite by molecular-beam epitaxy, *Nanoscale* **9**, 15945 (2017).
- [48] Y. X. Wang, G. Qiu, R. X. Wang, S. Y. Huang, Q. X. Wang, Y. Y. Liu, Y. C. Du, W. A. Goddard III, M. J. Kim, X. F. Xu, P. D. Ye, and W. Z. Wu, Field-effect transistors made from solution-grown two-dimensional tellurene, *Nat. Electron.* **1**, 228 (2018).
- [49] J. Peng, Y. Pan, Z. Yu, J. J. Wu, J. C. Wu, Y. Zhou, Y. Q. Guo, X. J. Wu, C. Z. Wu, and Y. Xie, Two-Dimensional Tellurium Nanosheets Exhibiting an Anomalous Switchable Photoresponse with Thickness Dependence, *Angew. Chem. Int. Ed.* **57**, 13533 (2018).
- [50] A. Apte, E. Bianco, A. Krishnamoorthy, S. Yazdi, R. Rao, N. Glavin, H. Kumazoe, V. Varshney, A. Roy, F. Shimojo, E. Ringe, R. K. Kalia, A. Nakano, C. S. Tiwary, P. Vashishta, V. Kochat, and P. M. Ajayan, Polytypism in ultrathin tellurium, *2D Mater.* **6**, 015013 (2019).

- [51] S. D. Kang, T. Dai, S. Dang, X. Y. Ma, G. L. Wang, H. W. Li, P. Hu, F. M. Yu, X. Zhou, S. X. Wu, S. W. Li, Broadband photoresponse of tellurium nanorods grown by molecular beam epitaxy, *Chem. Phys. Lett.* **729**, 49 (2019).
- [52] S. Deckoff-Jones, Y. X. Wang, H. T. Lin, W. Z. Wu, and J. J. Hu, Tellurene: A Multifunctional Material for Mid-infrared Optoelectronics, *ACS Photonics* **6**, 1632 (2019).
- [53] X. C. Huang, J. Q. Guan, Z. J. Lin, B. Liu, S. Y. Xing, W. H. Wang, and J. D. Guo, Epitaxial Growth and Band Structure of Te Film on Graphene, *Nano Lett.* **17**, 4619 (2017).
- [54] J. S. Qiao, Y. H. Pan, F. Yang, C. Wang, Y. Chai, and W. Ji, Few-layer tellurium: one-dimensional-like layered elementary semiconductor with striking physical properties, *Sci. Bull.* **63**, 159 (2018).
- [55] Y. Wang, C. C. Xiao, M. G. Chen, C. Q. Hua, J. D. Zou, C. Wu, J. Z. Jiang, S. Y. A. Yang, Y. H. Lu, and W. Ji, Two-dimensional ferroelectricity and switchable spin-textures in ultra-thin elemental Te multilayers, *Mater. Horiz.*, **5**, 521, (2018).
- [56] C. Wang, X. Y. Zhou, J. S. Qiao, L. W. Zhou, X. H. Kong, Y. H. Pan, Z. H. Cheng, Y. Chai, and W. Ji, Charge-governed phase manipulation of few-layer tellurium, *Nanoscale*, **10**, 22263, (2018).
- [57] W. D. Teuchert, R. Geick, G. Landwehr, H. Wendel, and W. Weber, Lattice dynamics of trigonal selenium. I. Phonon spectra, *J. Phys. C: Solid State Phys.* **8**, 3725 (1975).
- [58] R. Keller, W. B. Holzapfel, and H. Schulz, Effect of pressure on the atom positions in Se and Te, *Phys. Rev. B* **16**, 4404 (1977).
- [59] P. E. Blöchl, Projector augmented-wave method, *Phys. Rev. B* **50**, 17953 (1994).
- [60] G. Kresse and J. Furthmüller, Efficient iterative schemes for ab initio total-energy calculations using a plane-wave basis set, *Phys. Rev. B* **54**, 11169 (1996).
- [61] G. Kresse and J. Furthmüller, Efficiency of ab-initio total energy calculations for metals and semiconductors using a plane-wave basis set, *Comput. Mater. Sci.* **6**, 15 (1996).
- [62] J. P. Perdew, K. Burke, and M. Ernzerhof, Generalized Gradient Approximation Made Simple, *Phys. Rev. Lett.* **77**, 3865 (1996).
- [63] P. E. Blöchl, O. Jepsen, and O. K. Andersen, Improved tetrahedron method for Brillouin-zone integrations, *Phys. Rev. B* **49**, 16223 (1994).
- [64] J. W. Sun, A. Ruzsinszky, and J. P. Perdew, Strongly Constrained and Appropriately Normed Semilocal Density Functional, *Phys. Rev. Lett.* **115**, 036402 (2015).
- [65] H. W. Peng, Z.-H. Yang, J. P. Perdew, and J. W. Sun, Versatile van der Waals Density Functional Based on a Meta-Generalized Gradient Approximation, *Phys. Rev. X* **6**, 041005 (2016).
- [66] T. Thonhauser, V. R. Cooper, S. Li, A. Puzder, P. Hyldgaard, and D. C. Langreth, Van der Waals density functional: Self-consistent potential and the nature of the van der Waals bond, *Phys. Rev. B* **76**, 125112 (2007).
- [67] S. Grimme, Semiempirical GGA-Type Density Functional Constructed with a Long-Range Dispersion Correction, *J. Comput. Chem.* **27**, 1787 (2006).
- [68] G. Y. Guo and J. C. Lin, Systematic ab initio study of the optical properties of BN nanotubes, *Phys. Rev. B* **71**, 165402 (2005).
- [69] B. Adolph, J. Furthmüller, and F. Bechstedt, Optical properties of semiconductors using projector-augmented waves, *Phys. Rev. B* **63**, 125108 (2001).
- [70] A. M. Cook, B. M. Fregoso, F. de Juan, S. Coh, and J. E. Moore, Design principles for shift current photovoltaics, *Nat. Commun.* **8**, 14176 (2017).
- [71] H. C. Hsueh, G. Y. Guo, and S. G. Louie, Excitonic effects in the optical properties of a SiC sheet and nanotubes, *Phys. Rev. B* **84**, 085404 (2011).
- [72] D. Y. Qiu, F. H. da Jornada, and S. G. Louie, Optical Spectrum of MoS<sub>2</sub>: Many-Body Effects and Diversity of Exciton States, *Phys. Rev. Lett.* **111**, 216805 (2013).
- [73] Z. H. Levine and D. C. Allan, Quasiparticle calculation of the dielectric response of silicon and germanium, *Phys. Rev. B* **43**, 4187 (1991).
- [74] J. Heyd, G. E. Scuseria, and M. Ernzerhof, Hybrid functionals based on a screened Coulomb potential, *J. Chem. Phys.* **118**, 8207 (2003).
- [75] L. X. Benedict, E. L. Shirley, and R. B. Bohn, Theory of optical absorption in diamond, Si, Ge, and GaAs, *Phys. Rev. B* **57**, R9385 (1998).
- [76] T. Cheiwchanchamnangij and W. R. L. Lambrecht, Quasiparticle band structure calculation of monolayer, bilayer, and bulk MoS<sub>2</sub>, *Phys. Rev. B* **85**, 205302 (2012).
- [77] G. Shi and E. Kioupakis, Anisotropic Spin Transport and Strong Visible-Light Absorbance in Few-Layer SnSe and GeSe, *Nano Lett.* **15**, 6926 (2015).
- [78] Y. M. Fang, S. Q. Wu, Z.-Z. Zhu, and G.-Y. Guo, Large magneto-optical effects and magnetic anisotropy energy in two-dimensional Cr<sub>2</sub>Ge<sub>2</sub>Te<sub>6</sub>, *Phys. Rev. B* **98**, 125416 (2018).
- [79] M. Buscema, D. J. Groenendijk, S. I. Blanter, G. A. Steele, H. S. J. van der Zant, and A. Castellanos-Gomez, Fast and Broadband Photoresponse of Few-Layer Black Phosphorus Field-Effect Transistors, *Nano Lett.* **14**, 3347 (2014).
- [80] C. O. Kim, S. Kim, D. H. Shin, S. S. Kang, J. M. Kim, C. W. Jang, S. S. Joo, J. S. Lee, J. H. Kim, S.-H. Choi, and E. Hwang, High photoresponsivity in an all-graphene p – n vertical junction photodetector, *Nat. Commun.* **5**, 3249 (2014).
- [81] D. A. Nguyen, H. M. Oh, N. T. Duong, S. Bang, S. J. Yoon, and M. S. Jeong, Highly Enhanced Photoresponsivity of a Monolayer WSe<sub>2</sub> Photodetector with Nitrogen-Doped Graphene Quantum Dots, *ACS Appl. Mater. Interfaces* **10**, 10322 (2018).
- [82] E. P. Wu, D. Wu, C. Jia, Y. G. Wang, H. Y. Yuan, L. H. Zeng, T. T. Xu, Z. F. Shi, Y. T. Tian, and X. J. Li, In Situ Fabrication of 2D WS<sub>2</sub>/Si Type-II Heterojunction for Self-Powered Broadband Photodetector with Response up to Mid-Infrared, *ACS Photonics* **6**, 565 (2019).
- [83] X. T. Wang, Y. Cui, T. Li, M. Lei, J. B. Li, and Z. M. Wei, Recent Advances in the Functional 2D Photonic and Optoelectronic Devices, *Adv. Optical Mater.* **7**, 1801274 (2019).
- [84] A. Zenkevich, Y. Matveyev, K. Maksimova, R. Gaynutdinov, A. Tolstikhina, and V. Fridkin, Giant bulk photovoltaic effect in thin ferroelectric BaTiO<sub>3</sub> films, *Phys. Rev. B* **90**, 161409 (2014).
- [85] S. M. Young, F. Zheng, and A. M. Rappe, First-Principles Calculation of the Bulk Photovoltaic Effect in Bismuth Ferrite, *Phys. Rev. Lett.* **109**, 236601 (2012).
- [86] F. Zheng, H. Takenaka, F. Wang, N. Z. Koocher, and A. M. Rappe, First-Principles Calculation of the Bulk Pho-

- tovoltaic Effect in  $\text{CH}_3\text{NH}_3\text{PbI}_3$  and  $\text{CH}_3\text{NH}_3\text{PbI}_{3-x}\text{Cl}_x$ , *J. Phys. Chem. Lett.* **6**, 31 (2015).
- [87] X. X. Jiang, S. G. Zhao, Z. S. Lin, J. H. Luo, P. D. Bristowe, X. G. Guan, and C. T. Chen, The role of dipole moment in determining the nonlinear optical behavior of materials: ab initio studies on quaternary molybdenum tellurite crystals, *J. Mater. Chem. C* **2**, 530 (2014).
- [88] A. Cammarata, W. G. Zhang, P. S. Halasyamani, and J. M. Rondinelli, Microscopic Origins of Optical Second Harmonic Generation in Noncentrosymmetric-Nonpolar Materials, *Chem. Mater.* **26**, 5773 (2014).
- [89] J. Ingers, K. Maschke, and S. Proennecke, Optical-transition-matrix elements between localized electronic states in disordered one-dimensional systems, *Phys. Rev. B* **37**, 6105 (1988).
- [90] J.-H. Song, A. J. Freeman, T. K. Bera, I. Chung, and M. G. Kanatzidis, First-principles prediction of an enhanced optical second-harmonic susceptibility of low-dimensional alkali-metal chalcogenides, *Phys. Rev. B* **79**, 245203 (2009).